



ELSEVIER

Contents lists available at [ScienceDirect](http://www.sciencedirect.com)

## Journal of Sound and Vibration

journal homepage: [www.elsevier.com/locate/jsv](http://www.elsevier.com/locate/jsv)

# Optimization based determination of highly absorbing boundary conditions for linear finite difference schemes



A. Schirrer, E. Talic\*, G. Aschauer, M. Kozek, S. Jakubek

*Inst. of Mechanics & Mechatronics, Vienna University of Technology, Getreidemarkt 9, 1060 Vienna, Austria*

## ARTICLE INFO

*Article history:*

Received 8 April 2015

Received in revised form

1 December 2015

Accepted 2 December 2015

Handling Editor: I. Lopez Arteaga

Available online 19 December 2015

*Keywords:*absorbing boundary condition,  
wave propagation

## ABSTRACT

Many wave propagation problems (in acoustics or in railway catenary or cable car dynamics, for example) can be solved with high efficiency if the computational domain can be truncated to a small region of interest with appropriate absorbing boundary conditions. In this paper, highly absorbing and stable boundary conditions for linear partial differential equations discretized by finite difference schemes are directly designed using a flexible, optimization-based formulation. The proposed optimization approach to the computation of the absorbing boundary conditions is capable of optimizing the accuracy (the absorbing quality of the boundary condition) while guaranteeing stability of the discretized partial differential equations with the absorbing boundary conditions in place. Penalty functions are proposed that explicitly quantify errors introduced by the boundary condition on the solution of the bounded domain compared to the solution of the unbounded domain problem. Together with the stability condition the described approach can be applied on various types of linear partial differential equations and is thus applicable for generic wave propagation problems. Its flexibility and efficiency is demonstrated for two engineering problems: The Euler–Bernoulli beam under axial load, which can be used to model cables as well as catenary flexural dynamics, and a two-dimensional wave as commonly encountered in acoustics. The accuracy of the absorbing boundary conditions obtained by the proposed concept is compared to analytical absorbing boundary conditions.

© 2015 Elsevier Ltd. All rights reserved.

## 1. Introduction

Many physical applications that show wave propagation phenomena, such as pressure waves in fluids, acoustic problems, or vibrations in strings and beams, are modeled by partial differential equations (PDEs) on bounded domains (clamped beam, sound waves in a chamber) or unbounded domains (long cables or catenaries, free sound wave propagation). To approximate the analytical solution the PDE is often discretized over a limited computational domain although the original problem may be defined on a much larger space. In order to obtain a well-posed problem suitable boundary conditions (BCs) and initial conditions (ICs) are needed. Choosing simple homogeneous BCs (Dirichlet/Neumann BCs respectively clamped BCs) is unsuitable in this setting because they fully reflect outgoing waves back into the domain. To avoid such spurious reflections into the domain of interest, the computational domain would have to be vastly expanded which

\* Corresponding author. Tel.: +43 158801 325524.

E-mail addresses: [alexander.schirrer@tuwien.ac.at](mailto:alexander.schirrer@tuwien.ac.at) (A. Schirrer), [emir.talic@tuwien.ac.at](mailto:emir.talic@tuwien.ac.at) (E. Talic), [guilherme.aschauer@tuwien.ac.at](mailto:guilherme.aschauer@tuwien.ac.at) (G. Aschauer), [martin.kozek@tuwien.ac.at](mailto:martin.kozek@tuwien.ac.at) (M. Kozek), [stefan.jakubek@tuwien.ac.at](mailto:stefan.jakubek@tuwien.ac.at) (S. Jakubek).

drastically increases computational effort. Special so-called absorbing boundary conditions (ABCs) [1] have been proposed which ideally absorb outwards-traveling waves without reflections or the need to expand the computational domain. However, the analytic formulation of ABCs is not straightforward at all and heavily depends on the underlying PDE.

The finite difference (FD) method is one widely used technique to approximate the solution of the continuous PDE problem [2]. Its simple and flexible formulation relies on approximating the occurring partial derivatives by, for example, central differences, yielding an algebraic set of equations whose solution approximates the PDE's solution.

In this paper, an optimization-based method to obtain the unknown coefficients of a general explicit linear stencil for an ABC in the fully time/space-discretized FD problem is proposed. The method is illustrated by two examples – the Euler–Bernoulli beam (EBB) equation under axial load as well as the two-dimensional scalar wave equation.

ABCs for the wave equation have been investigated over the last decades. Well-known ABC formulations were developed by Engquist and Majda [3] and by Bayliss and Turkel [4]. The first approach is based on a factorization of the wave equation and leads to a non-local ABC, which must be transformed to a local ABC using pseudo-differential calculus in combination with truncated Taylor series, and the latter is based on a far-field asymptotic solution of the wave equation [5]. In Ref. [6] ABCs are developed for the FD approximation of a two-dimensional wave equation using the discrete dispersion relation. The same author developed radiation BCs for elastic and dispersive waves in the Refs. [7] and [8], respectively. Improvements led to local high-order ABCs [9], which have been applied on different types of wave equations, such as the time-dependent [10] and dispersive [11] cases. A review on high-order ABCs can be found in Givoli [12]. A different approach is the formulation of absorbing layers that expand the computational domain by an area with dissipating properties. These so-called sponge layers increase the damping in the absorbing layer to attenuate incident waves and can also be combined with ABCs [13]. In Ref. [14] sponge layers were used for the aeroacoustic time-reversal method to localize sound sources. A more advanced approach is the Perfectly Matched Layer (PML) [15] which uses a complex change of coordinates [16] to achieve high absorption performance, however at the cost of a considerable number of additional equations and variables to be solved in a time-marching scheme. The authors of Ref. [17] adopted the PML from Ref. [15] for the transition line method. The close relation of ABCs and PMLs is discussed in Ref. [9], and a combination of ABCs and PMLs has recently been presented in Hagstrom [18]. A historical overview on ABCs and PMLs is given in Berenger [19].

Developments related to ABCs for the EBB have been made in the field of boundary control of PDEs [20,21]. However, in Ref. [20] no axial load was considered when ABCs for the EBB were derived. The authors of Ref. [22] have successfully applied boundary control on an axially moving EBB under axial load, but their goal was to suppress vibrations by maximizing damping and energy absorption. In the present paper, ABCs for the FD-discretized EBB equation will be generated (in contrast to Ref. [20] an axial load is considered here). The goal of the optimized ABCs is to approximate the unbounded domain solution (not absorb energy as fast as possible as done in Lee [22]).

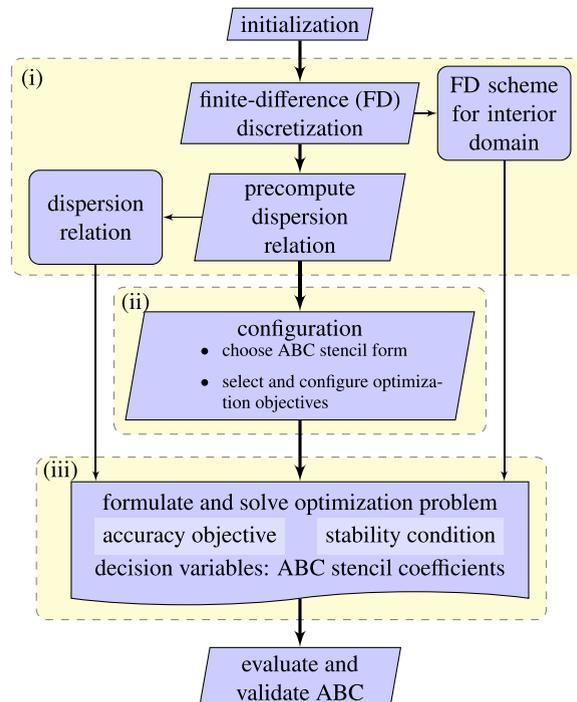


Fig. 1. Block diagram of the proposed method to obtain optimized ABC stencil coefficients.

The main contributions of this work are (a) a generic optimization approach to the determination of the ABC; (b) two accuracy objectives as well as one stability condition to allow the optimization to be carried out for generic wave propagation problems; and (c) the demonstration of the proposed method for two common engineering problems: the EBB equation *under axial load*, which to the best authors' knowledge has not yet been investigated in terms of ABCs in this configuration, and the two-dimensional scalar wave equation.

In contrast to the approaches available in literature, where the ABCs are typically developed for a specific PDE (and often in the continuous domain), here a generic method is proposed to directly obtain discrete ABC realizations for given discretization schemes of PDEs. This is done intentionally to avoid additional errors produced by discretizing a continuous ABC. Also, the method is generic in the sense that any large-scale reference system's solution could be utilized to fit the truncated system's response to. However, we make some basic assumptions in order to exploit problem structure and improve the method's efficiency. These assumptions are the PDE is linear with constant coefficients, has no (or, sufficiently low) damping, has a *harmonic traveling wave solution* [23,24], and its so-called *discrete dispersion relation* [6] can be derived (see Section 2.4).

The proposed optimization approach (main contribution (a)) consists of three major steps ((i), (ii) and (iii)) as illustrated in Fig. 1.

In step (i) the investigated PDE is approximated by standard central differences [25] using evenly spaced grids in space and time directions to obtain a set of algebraic equations. We denote the range of grid points that can be approximated by central differences as *interior domain* and the remaining grid points as *boundary points*. Each algebraic equation describes a relation between the unknown future (one-step-ahead) values and the known values of the solution. The pattern of these relations of points in the space–time grid is called *stencil* and the corresponding coefficients are called *stencil coefficients*. To perform numerically stable simulations the constant distances between two grid points in time and space directions – the so-called *step sizes* – have to be chosen appropriately. This choice of the space and the time step size is common to all FD problems and is, for example, guided by the von Neumann stability analysis or the Courant–Friedrich–Lewy's condition [2]. At this point, the dispersion relation can be precomputed and stored.

In step (ii) first the form of the ABC *stencil* for the boundary points has to be chosen. This choice is problem-dependent and may require a priori knowledge of the physical conditions under which the problem needs to be solved. Various stencil forms can be tested and optimized to obtain the best performing out of a limited number of candidates. For each time and space step size couple  $\{\Delta t, \Delta x\}$  the ABC stencil has to be recomputed (or stored in advance) before running a simulation. Then an accuracy objective and a stability condition are selected and configured.

In step (iii) the optimization problem with the stencil coefficients as *decision variables* is formulated. One way is to set-up a single-objective optimization where just the accuracy of the ABCs is improved and stability is enforced through imposing a constraint. Standard single-objective optimization methods [26] such as pattern search [27] can then be utilized. The other possibility is to consider a multi-objective optimization (MOO) problem and to treat accuracy and stability as conflicting objectives. The MOO problem can, for example, be solved by population-based algorithms such as multi-objective genetic algorithms [28,29]. It is noted that population-based methods offer a set of solutions after the optimization which shows efficient trade-offs (of accuracy vs. stability). Either way, each solution defines a set of ABC stencil coefficients which directly constitute an ABC realization.

Two accuracy objectives and a stability condition are proposed (main contribution (b)). The first accuracy objective, here denoted as *reflection error*, expresses the magnitude of the reflection coefficient (RC) [30], which is ideally zero for all frequencies fulfilling the discrete dispersion relation of the interior domain stencil. The second proposed accuracy objective quantifies the amount of reflections of the harmonic wave solution of the FD scheme by the ABCs in an *output-error* sense [31].

In Refs. [32–34] FD-ABCs were used to stabilize simulations of wave propagation phenomena on unbounded domains over long time durations. To verify stability, eigenvalue analyses have been carried out in these references. However, the authors observed that optimizing ABCs using direct optimization (with accuracy objectives only) may lead to ABCs stencils that destabilize the system. Similar observations – concerning long-duration instabilities – have been made by Rabinovich in Ref. [35] in the field of elastodynamics for analytically derived ABCs. These instabilities have been delayed by introducing numerical damping in the same paper and eliminated by using special operators in Ref. [36]. In this paper, we adopt the eigenvalue analysis of the Refs. [32–34] for a fully discretized PDE. On that basis a stability objective evaluates the locations of the eigenvalues of a sufficiently large test system in state-space representation with the ABCs in place. In order to obtain an asymptotically stable FD scheme, all eigenvalues of the corresponding system matrix must lie inside the unit circle (see e.g. Ref. [37]).

The outline of this paper is: First, the basic effect of ABCs compared to standard Dirichlet and Neumann BCs is shown for the EBB under axial load by simulation. The influence of the two proposed accuracy objectives on the actual absorption properties is discussed, the choice of a stability objective vs. constraint is discussed, and the influence of frequency-weighting of the accuracy objective on the obtained ABC behavior is illustrated. Furthermore eigenvalue and sensitivity analyses will be performed for the one-dimensional case. The second example highlights the proposed method on the two-dimensional wave equation where the ABC stencil coefficients are optimized for certain angles of incidence and frequencies. The method is compared with the well-known Engquist–Majda-ABCs from Ref. [3].

## 2. Finite difference approximation of PDEs

The proposed method for obtaining the ABCs as an output of an optimization problem is directly applicable to PDEs being linear with constant coefficients, having no damping terms and for which harmonic traveling wave solutions exist (see Section 2.4). Additionally, some basic analytical treatment of the underlying PDE is performed. The necessary steps will be illustrated for the case of the EBB in this section, but are easily applicable to other PDEs modeling wave propagation phenomena. Furthermore, it is assumed that the update equation for the future time step can be written in an explicit form.

### 2.1. EBB under axial load

The PDE describing the dynamic behavior of a homogeneous EBB under axial load without damping is given by [38]

$$\rho A \frac{\partial^2 u}{\partial t^2} = -EI \frac{\partial^4 u}{\partial x^4} + T \frac{\partial^2 u}{\partial x^2},$$

$$u = u(x, t), \quad x \in [0, L] \subseteq \mathbb{R}, \quad t \in \mathbb{R}^+ \cup \{0\}, \tag{1}$$

where the constant coefficients are the axial load  $T$ , the mass per unit length  $\rho A$ , and the bending stiffness  $EI$ . The spatial variable is  $x$ , time is denoted by  $t$ , and the beam length is  $L$ .  $u(x, t)$  denotes the vertical displacement of the beam.

### 2.2. Approximation of the interior domain

To numerically solve a PDE with the FD method the partial derivatives have to be approximated. To do so, the solution domain is divided into a uniform grid in space and time:  $x \times t = [0, \Delta x, \dots, N_x \Delta x] \times [0, \Delta t, \dots, N_t \Delta t]$ . Consequently, the variable  $u(x, t)$  is only defined at each grid point ( $u(x_k, t_n) = u_k^n$ ). The partial derivatives in (1) can then, for example, be approximated by finite differences [25]:

$$\frac{\partial^2 u}{\partial x^2}(x_k, t_n) \approx \frac{u_{k-1}^n - 2u_k^n + u_{k+1}^n}{\Delta x^2}, \tag{2a}$$

$$\frac{\partial^2 u}{\partial t^2}(x_k, t_n) \approx \frac{u_k^{n-1} - 2u_k^n + u_k^{n+1}}{\Delta t^2}, \tag{2b}$$

$$\frac{\partial^4 u}{\partial x^4}(x_k, t_n) \approx \frac{u_{k-2}^n - 4u_{k-1}^n + 6u_k^n - 4u_{k+1}^n + u_{k+2}^n}{\Delta x^4}. \tag{2c}$$

Using central differences leads to symmetric stencil coefficients and it is assumed that the update equation producing the solution at each grid point for the next time step can explicitly be written as

$$u_k^{n+1} = \sum_{i=0}^{N_t^{\text{INT}}-1} \sum_{j=-(N_x^{\text{INT}}-1)/2}^{(N_x^{\text{INT}}-1)/2} a_j^i u_{k+j}^{n-i}, \tag{3}$$

which is the case for central differences if no mixed derivatives appear in the PDE. Thereby,  $a_j^i$  are the stencil coefficients (see Fig. 2) and  $N_t^{\text{INT}}, N_x^{\text{INT}}$  are the numbers of time steps and spatial values needed to obtain the next solution value, respectively. In case of the EBB PDE (1), discretized with central differences (2),  $N_t^{\text{INT}} = 2$  and  $N_x^{\text{INT}} = 5$  hold. The coefficients  $a_j^i$  of (3) for the

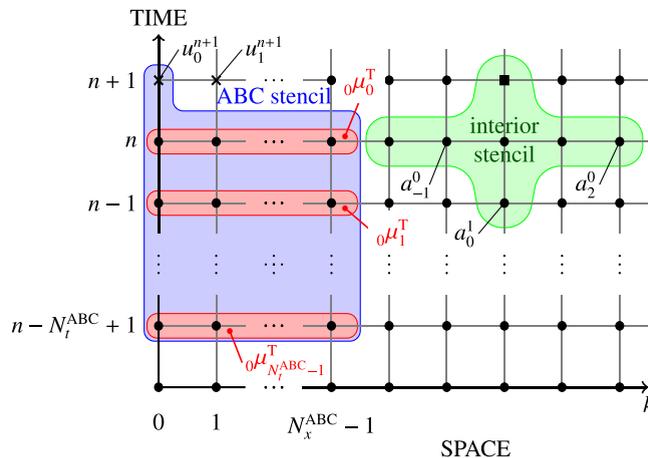


Fig. 2. Generic form of an explicit boundary condition stencil for  $k=0$  (left) and an explicit interior stencil (right).

EBB PDE (1) are:

$$\begin{aligned}
 a_{\pm 2}^0 &= -\frac{EI \Delta t^2}{\rho A \Delta x^4}, & a_{\pm 1}^0 &= \frac{\Delta t^2 (4 EI + T \Delta x^2)}{\rho A \Delta x^4}, \\
 a_0^0 &= \frac{-6 EI \Delta t^2 - 2 T \Delta x^2 \Delta t^2 + 2 \rho A \Delta x^4}{\rho A \Delta x^4}, \\
 a_0^1 &= -1, & a_{\pm 1}^1 &= a_{\pm 2}^1 = 0.
 \end{aligned}
 \tag{4}$$

An example of such interior stencil structure is shown on the right side in Fig. 2.

### 2.3. Bounds for the time step size $\Delta t$

The FD scheme obtained above is conditionally stable [25]. For given physical parameters and spatial step size  $\Delta x$ , the time step size needs to fulfill  $\Delta t \leq \Delta t_{\max}$  to result in a stable scheme where numeric errors are not amplified over time. In case of a linear PDE with constant coefficients defined on an unbounded domain, the von Neumann stability analysis [25] can be applied to obtain this maximal time step size  $\Delta t_{\max}$ . For the EBB PDE (1) discretized by central differences (2), the following bound is obtained:

$$\Delta t_{\max} = \sqrt{\frac{\Delta x^4}{\frac{T}{\rho A} \Delta x^2 + 4 \frac{EI}{\rho A}}}.
 \tag{5}$$

**Remark 1.** It is noted that  $\Delta t_{\max}$  denotes a stability bound for the explicit FD time-marching scheme for the unbounded domain. Thus, the spatial and temporal step sizes are chosen a priori and are kept fixed during the optimization. To verify stability of the system with ABCs in place an eigenvalue analysis is performed (see Section 3.3). Moreover, Eq. (5) matches exactly the Courant–Friedrich–Lewy’s condition (see Ref. [39]) for  $EI=0$ .

### 2.4. Dispersion relation

For a PDE with traveling-wave-solutions the so-called *dispersion relation* on an unbounded domain can be derived if a harmonic wave of the form [23]

$$u(x, t) = e^{I(\omega_x x + \omega_t t)}
 \tag{6}$$

is a solution of the homogeneous PDE, where  $I$  is the imaginary unit and  $\omega_x, \omega_t \in \mathbb{R}$ . It is noted that this corresponds to an oscillatory traveling wave solution of an undamped problem. The dispersion relation describes the connection between the spatial frequency or wave number  $\omega_x \in \mathbb{R}$  (or the wave vector  $k = [\omega_x, \omega_y, \dots]^T$  in the higher-dimensional case) and the temporal frequency  $\omega_t \in \mathbb{R}$ . The general form of this relation is

$$f(\omega_t, \omega_x) = 0.
 \tag{7}$$

Likewise, using the discrete counterpart of (6),

$$u_k^n = (e^{I\omega_x \Delta x})^k (e^{I\omega_t \Delta t})^n = \kappa^k \tau^n,
 \tag{8}$$

the so-called *discrete dispersion relation* [6] can be derived by substituting (8) into an FD-discretized PDE.

To shorten notation, the dependency of  $\kappa$  and  $\tau$  on  $\omega_x$  and  $\omega_t$ , respectively, will not be explicitly written in the remainder of the paper. Also it is noted that because of the linearity of the PDEs under investigation, the sum of harmonic waves is again a solution, hence the full solution can be written as a superposition of (infinitely) many harmonic wave solutions. Here, evanescent modes are not considered relevant in the formulation of ABC accuracy (as also argued in [11]).

For the EBB the discrete dispersion relation is obtained by combining (3), (4) and (8) and leads after simplifications to:

$$\sin^2\left(\frac{\omega_t \Delta t}{2}\right) = \frac{T \Delta t^2}{\rho A \Delta x^2} \sin^2\left(\frac{\omega_x \Delta x}{2}\right) + \frac{EI \Delta t^2}{\rho A \Delta x^4} \sin^4\left(\frac{\omega_x \Delta x}{2}\right).
 \tag{9}$$

### 2.5. Boundary conditions

In order to obtain a well-posed PDE problem, suitable initial conditions (ICs) and BCs are needed. These ICs and BCs have to be discretized as well if the solution is approximated using discrete numerical methods such as FD.

Fig. 2 shows a possible computation grid where an interior stencil is shown on the right side. This stencil cannot be used to compute the solution values at the boundary because it would rely on undefined grid points outside the computational domain. The number of boundary grid points  $N_{\text{ABC}}$  to compute depends on the spatial width of the interior stencil. For the explicit computation of the boundary grid points a generic explicit ABC stencil (on the left of Fig. 2) is introduced (here,

shown for the left boundary formulation throughout):

$$u_k^{n+1} = \sum_{i=0}^{N_t^{ABC}-1} k \mu_i^T \begin{bmatrix} u_0^{n-i} \\ \vdots \\ u_{N_x^{ABC}-1}^{n-i} \end{bmatrix}, \quad k = 0, \dots, N_{ABC}-1, \quad (10)$$

where  $k \mu_i^T \in \mathbb{R}^{N_x^{ABC}}$  denotes the vector of stencil coefficients for the  $(n-i)$ th time instant needed for the computation of the  $k$ th spatial grid point's value.  $N_t^{ABC}$  is the number of time instants that are needed for the ABC stencil computation and  $N_{ABC}$  is the number of boundary grid points. ABC stencils on the right boundary are defined analogously by spatially mirroring the entries of  $k \mu_i^T$ .

### 3. Methodology

#### 3.1. Basic considerations

Unlike the common approaches in the literature, where the ABCs are derived by physical considerations, in this work the determination of the stencil coefficients of the ABCs is formulated as an optimization problem. Therefore, two different accuracy objectives and one stability condition are introduced. Only taking accuracy objectives into account may lead to well-performing ABCs that, however, possibly introduce unstable dynamics. In these cases a stable parameter set can be enforced by adding a stabilizing objective or a stabilizing constraint. On the one side, using a stabilizing constraint a single objective optimization problem occurs and its solution is a stable candidate (ABC stencil). Depending on the single-objective optimization method and the starting point of the optimization a global minimum of the accuracy objective can be obtained. On the other side, formulating a stabilizing objective instead results in a MOO problem. Its solution is a set of candidates, where accuracy and stability can be traded against each other. Additionally, a number of different stencil forms can be tested and the trade-off between complexity, accuracy, and stability margin becomes clearly visible.

Moreover, the accuracy objectives can include weighting functions, introducing additional design degrees of freedom and thus the possibility to optimize the ABCs for specific application needs. Examples are the frequency of waves or the angle of incidence of waves reaching the boundary for the two-dimensional wave equation.

The proposed objective functions will be shown and derived for the one-dimensional case to simplify notation. However, their generalization to the higher-dimensional case is straightforward and will be sketched in Section 4.2.1.

#### 3.2. Accuracy objectives

Two accuracy objectives are proposed that are based on the error made at the boundary with respect to the outgoing harmonic wave solutions, and thus they quantify the difference between the bounded and unbounded domain solutions.

##### 3.2.1. Accuracy objective – reflection coefficient (RC)

The reflection coefficient (RC) was introduced in Ref. [6] to describe the reflection properties of ABCs. The derivation of the RC will be outlined here and extended for arbitrary boundary points  $u_k^{n+1}$ , with  $k = 0, \dots, N_{ABC}-1$ . The basic idea is to

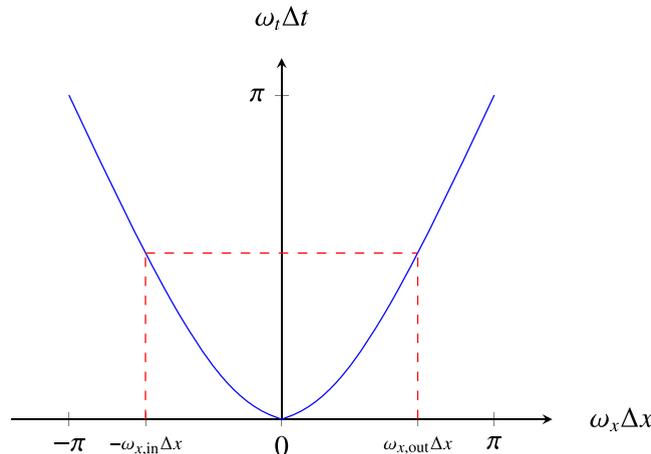


**Fig. 3.** The discrete dispersion relation for EBB equation for positive  $\omega_t \Delta t$  with  $EI = 150 \text{ N m}^2$ ,  $T = 15,000 \text{ N/m}$ ,  $\rho A = 1 \text{ kg/m}$ ,  $\Delta t = 9.9 \times 10^{-5} \text{ s}$  and  $\Delta x = 0.05 \text{ m}$ .

consider boundary conditions of the following form:

$$B_k(\tau, \kappa)u_k^{n+1} = 0, \quad k = 0, \dots, N_{ABC} - 1 \quad (11)$$

$B_k(\tau, \kappa)$  is obtained by inserting (8) into (10) and expressing the boundary point of interest. This leads to

$$B_k(\tau, \kappa) = 1 - \sum_{n=0}^{N_{ABC}^{ABC} - 1} k \mu_n^T \begin{bmatrix} \tau^{-(n+1)} \kappa^{-k} \\ \tau^{-(n+1)} \kappa^{-k+1} \\ \vdots \\ \tau^{-(n+1)} \kappa^{-k+N_{ABC}^{ABC} - 1} \end{bmatrix}. \quad (12)$$

To study the reflection properties, one considers the linear combination

$$u_k^n = c_{in} \kappa_{in}^k \tau^n + c_{out} \kappa_{out}^k \tau^n \quad (13)$$

where  $\kappa_{in}^k = \exp(i\omega_{x,in}\Delta x)$  and  $\kappa_{out}^k = \exp(i\omega_{x,out}\Delta x)$  are chosen to correspond with the incoming and outgoing wave components (understood as having positive and negative group velocities, respectively [6]) with amplitudes  $c_{in}$  and  $c_{out}$ . The spatial frequencies  $\omega_{x,in}$  and  $\omega_{x,out}$  are obtained from the discrete dispersion relation (7). The discrete dispersion relation for the EBB (9) is displayed in Fig. 3. The  $\omega_t \Delta t(\omega_x \Delta x)$ -branch with different signs of  $\omega_t \Delta t$  and  $\omega_x \Delta x$  represents the incoming and the branch with the same sign the outgoing wave components, with positive and negative group velocities, respectively. The group velocity is defined as

$$v_{group} = -\frac{\partial \omega_t}{\partial \omega_x}. \quad (14)$$

Finally, one obtains the RC by inserting (12) into (13) which leads to

$$c_{in} B_k(\tau, \kappa_{in}) + c_{out} B_k(\tau, \kappa_{out}) = 0 \quad (15)$$

or

$$c_{in} = - \underbrace{\frac{B_k(\tau, \kappa_{out})}{B_k(\tau, \kappa_{in})}}_{R_k(\omega_t \Delta t, \omega_x \Delta x)} c_{out}. \quad (16)$$

with the RC  $R_k$ . It is evident that the RC is a function of  $\kappa$  and  $\tau$  and is evaluated for certain pairs of  $(\omega_t \Delta t, \omega_x \Delta x)$ , which are related by the discrete dispersion relation. The goal for the optimization is to minimize  $|R_k|$ . Consequently, the first proposed accuracy criterion aggregates (16) over all relevant frequencies  $\omega_x \in [0, \pi/\Delta x]$  (up to the Nyquist frequency) with a user-defined frequency weighting  $w(\omega_x) \geq 0$ :

$$J_{perf,RC} = \sum_{k=0}^{N_{ABC}^{ABC} - 1} \int_0^{\pi/\Delta x} w(\omega_x) |R_k(\omega_x)| d\omega_x. \quad (17)$$

In the particular cases of the EBB and the two-dimensional wave equation the dispersion relation is symmetric with respect to the  $\omega_t$ -axis (see Fig. 3) and  $\omega_x = -\omega_{x,in} = \omega_{x,out}$ . Thus, the integral in (17) needs only be evaluated in the given interval.

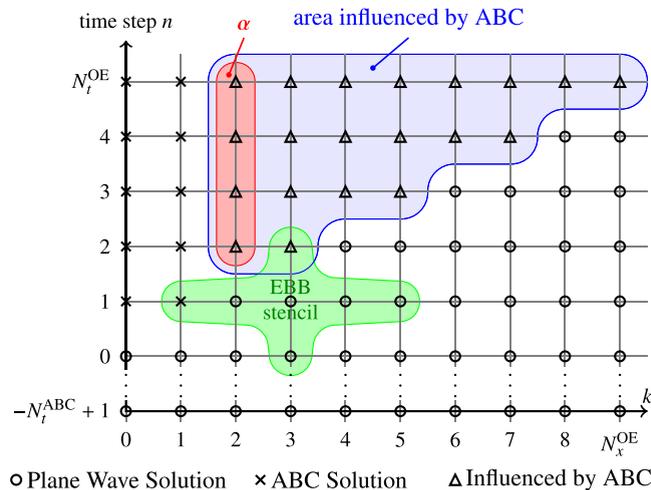


Fig. 4. Influence of an ABC stencil for the EBB into the interior domain.

### 3.2.2. Accuracy objective – output-error (OE)

The second proposed accuracy objective is based on simulating a harmonic wave solution on a (small) test domain with ABCs in place for several time steps and comparing a selected region of the solution to that of the unbounded domain which is directly available from (8). While the RC accuracy objective (16) minimizes the reflection of the boundary points for the frequency pairs  $(\omega_t, \omega_x)$  of the discrete dispersion relation (7), the OE accuracy objective minimizes the harmonic wave solution error in an output-error sense [31]. The concept behind the OE accuracy objective is sketched in Fig. 4 for the example of an EBB explicit interior stencil. Each grid point  $u_k^n$  at the time instants  $n = 0, -1, \dots, -N_t^{ABC} + 1$  is initialized with the harmonic wave solution (8). These grid points are marked by circles ( $\circ$ ). The boundary grid points (see Fig. 4,  $k = 0, 1$ ) where the solution is computed using the ABC stencils are indicated by crosses ( $\times$ ). Grid points that are influenced by boundary point values are marked by triangles ( $\Delta$ ) in Fig. 4. The idea is to minimize the difference of the solution marked with  $\Delta$  or a restricted area (e.g.  $\alpha$  with  $k = 2$  in Fig. 4) and the harmonic wave solution (8) on the unbounded domain. The output error of one harmonic wave solution is thus expressed as

$$e_{OE} = \sum_{n=2}^{N_t^{OE}} \sum_{k=2}^{N_x^{OE}} \left| u_k^n - \kappa^k e^n \right|^2, \quad (18)$$

and the solutions  $u_k^n$  are obtained from numeric solution of the test system. It is noted that the solution is let to evolve over  $N_t^{OE}$  time steps (in contrast to the 1-step evaluation of the RC accuracy objective (17)). The proposed OE objective again is obtained by aggregating the error function (18) over frequency:

$$J_{\text{perf,OE}} = \int_0^{\pi/\Delta x} w(\omega_x) e_{OE}(\omega_x) d\omega_x. \quad (19)$$

### 3.3. Stability condition

Eq. (5) stated the von Neumann (Fourier) stability criterion for the EBB as an upper bound on the step size  $\Delta t$  to guarantee a stable FD scheme on an unbounded domain. Specific BCs can, however, still introduce instability. Therefore, a dedicated stability condition is introduced.

This stability condition evaluates the eigenvalues of the state-space system associated to an FD-approximated test system with applied ABCs. Every solution value at the time instant  $n$  is collected into

$$\mathbf{u}^n = \left[ u_0^n, u_1^n, \dots, u_{N_x-1}^n \right]^T. \quad (20)$$

Since there are two time steps involved in (4) for the EBB and possibly more for the ABC stencil (10), the state vector has to contain earlier values as well, depending on the highest number  $N_t^{\text{up}}$  of time steps appearing in the update equations:

$$\mathbf{v}^n = \left[ (\mathbf{u}^n)^T, (\mathbf{u}^{n-1})^T, \dots, (\mathbf{u}^{n-N_t^{\text{up}}+2})^T \right]^T. \quad (21)$$

This augmented state vector then consists of  $(N_t^{\text{up}} - 1)N_x$  elements and the update equation can be written in the following form:

$$\mathbf{v}^{n+1} = \mathbf{A}\mathbf{v}^n, \quad (22)$$

with the discrete-time system matrix  $\mathbf{A} \in \mathbb{R}^{((N_t^{\text{up}} - 1)N_x) \times ((N_t^{\text{up}} - 1)N_x)}$ , incorporating the discretized PDE (3), as well as the update equation (10) for the boundary grid points and the past time steps  $\mathbf{u}^{n-1}, \dots, \mathbf{u}^{n-N_t^{\text{up}}+2}$ .

The solution eigendynamics on each grid point is entirely described by  $\mathbf{A}$  and linear system theory can readily be applied to study stability. In fact, a discrete-time system of the form (22) is asymptotically stable if and only if all eigenvalues of the state matrix  $\mathbf{A}$  lie within the unit circle, i.e. have magnitude smaller than one [37], leading to the stability constraint

$$\rho(\mathbf{A}) = \max_i |\lambda_i(\mathbf{A})| < 1, \quad (23)$$

which can also be addressed in the optimization in the form of a stability objective:

$$J_{\text{stab}} = \rho(\mathbf{A}). \quad (24)$$

It is noted that the value  $J_{\text{stab}} < 1$  corresponds to a positive stability margin and quantifies the global exponential decay rate. The accuracy/stability margin trade-off is made visible by taking on the MOO formulation. Furthermore, this condition evaluates asymptotic stability for a concrete implementation. However, it is assumed that the stability properties of the boundary region affect small and large systems in the same way which has been empirically observed by the authors.

For the undamped wave and EBB PDEs, central differences with applied Dirichlet/Neumann BCs lead to a unimodal system (all eigenvalues have magnitude one), independent of the number of interior grid points.

**Remark 2.** The ABC stencils may also be formulated implicitly, leading additionally to stencil coefficients  ${}_k\mu_1^T$  on the left hand side of Eq. (10). Consequently this leads to an implicit state space representation  $\mathbf{M}\mathbf{v}^{n+1} = \mathbf{A}\mathbf{v}^n$  (compare Eq. (22)).

### 3.4. Single-objective optimization

By choosing one of the accuracy objectives (17) or (19) together with the stability constraint (24), a suitable optimization problem for the determination of well-performing and stable ABCs can be stated. Mathematically, a parameter vector  $\mathbf{p} = \{\mu_i\}$ ,  $k = 0, \dots, N_{\text{ABC}} - 1$ ,  $i = 0, \dots, N_t^{\text{ABC}} - 1$ , consisting of the  $N_p = N_{\text{ABC}} \times N_t^{\text{ABC}} \times N_x^{\text{ABC}}$  stencil coefficients in the  $\mu_i^T$  vectors of (10) is sought that minimizes a cost function  $J = J_{\text{perf}}(\mathbf{p})$ :

$$\begin{aligned} & \min_{\mathbf{p}} J(\mathbf{p}) \\ & \text{subject to } \rho(\mathbf{A}) < 1 \end{aligned} \tag{25}$$

where  $\mathbf{p} \in \mathbb{R}^{N_p}$  and  $J \in \mathbb{R}$ . In this work a pattern-search algorithm [27] was utilized for solving the optimization problem. Pattern-search belongs to the class of gradient-free optimization methods but only one solution candidate is considered. This solution is iteratively improved by evaluating the objective function in its neighborhood at points having a fixed distance to the current solution, called mesh size. If a better point is found, it is denoted as the new solution and the mesh size is doubled (exploration). If, after evaluating the neighborhood, the current point is still optimal, the mesh size is reduced (intensification). This process is repeated until the mesh size reaches a lower tolerance value.

### 3.5. Multi-objective optimization (MOO)

By incorporating the stability objective (24) into the optimization problem and treating it equally to the accuracy objective MOO results. Stencil coefficients are sought that minimize a vector-valued cost function  $\mathbf{J} = [J_{\text{perf}}(\mathbf{p}), J_{\text{stab}}(\mathbf{p})]^T$  in the Pareto sense [40]:

$$\min_{\mathbf{p}} \mathbf{J}(\mathbf{p}), \quad \mathbf{p} \in \mathbb{R}^{N_p}, \quad \mathbf{J} \in \mathbb{R}^2. \tag{26}$$

Typically, the two objectives are conflicting. Each solution candidate that cannot be further improved in one objective without deteriorating the other objective is called Pareto optimal [28]. The result of the MOO problem solved by population-based approaches is an approximation of the Pareto-optimal solution set (called Pareto front). In this work the MOO problem (26) is solved by a multi-objective genetic algorithm (NSGA-II [29]). Genetic algorithms belong to the class of evolutionary algorithms and are inspired by nature's evolution process. They use a set of solution candidates, called *population*, and improve it iteratively. Each iteration, called *generation*, is evolved by the operations *selection*, *recombination*, and *mutation*. Initial solutions can be obtained by single-objective optimization, via randomization, or by using already known ABCs.

## 4. Numerical results

Using an EBB test system, a simulation run illustrates the wave absorption with an ABC in place. The two accuracy objectives will be compared and their properties discussed. Furthermore, the frequency-weighting of the accuracy objectives and its influence on the time-domain results will be illustrated. For the two-dimensional wave equation first the ABC optimization method is adopted to the two-dimensional case and the optimized ABCs are compared with the second-order Engquist–Majda ABCs.

### 4.1. ABCs for the Euler–Bernoulli Beam (EBB) equation under axial load

The EBB model plays an important role in modeling bending beam dynamics. Its applications are found, for example, in cable car and railway catenary dynamics. Furthermore, the EBB equation is particularly challenging because physical dispersion is significant.

#### 4.1.1. EBB parameters and system setup

For the following studies the coefficients of the EBB equation (1) were chosen corresponding to typical high-speed railway catenary contact wire parameters [41]:

$$T = 1.5 \times 10^4 \text{ N}, \quad \rho A = 1 \text{ kg/m}, \quad EI = 150 \text{ N m}^2,$$

and the beam length is chosen with  $L = 100$  m. The simulation setup is structured as follows: ABC stencils are placed at the left boundary ( $x=0$  m) and a clamping BC was chosen for the right boundary ( $x=L$ ). The homogeneous clamping BC is here defined as

$$u(L, t) = 0, \quad \frac{\partial u}{\partial x}(L, t) = 0, \tag{27}$$

and can be realized by using FDs as

$${}_{N_x} \mu_0^T = [0 \ 0 \ 0 \ 0], \quad {}_{N_x-1} \mu_0^T = [0 \ 0 \ 0 \ 0]. \tag{28}$$

Because of the fourth derivative in the EBB PDE (1) which is discretized by (2), two boundary grid points on each side arise, and so two ABC stencils need to be optimized. The stencil size parameters of the ABCs are chosen as  $N_x^{ABC} = 4$  and  $N_t^{ABC} = 1$  (see Fig. 2). Furthermore, the spatial step size of the computational grid was chosen with  $\Delta x = 0.05$  m, and  $\Delta t = \Delta t_{max} = 9.9 \times 10^{-5}$  s was determined from (5). The simulation runs are started with the ICs

$$u(x, 0) = \begin{cases} \sin^2\left(\pi\left(\frac{x-x_c}{d} - \frac{1}{2}\right)\right) & -\frac{d}{2} \leq x-x_c \leq \frac{d}{2} \\ 0 & \text{elsewhere,} \end{cases} \quad (29a)$$

$$\frac{\partial u}{\partial t}(x, 0) = 0, \quad (29b)$$

with  $x_c = 25$  m and  $d = 0.5$  m. The IC is displayed in Fig. 5 as the topmost curve.

**Remark 3.** Setting  $\Delta t = \Delta t_{max}$  may cause numerical problems as floating point computations made by computers during the simulations can introduce small errors possibly leading to  $\Delta t > \Delta t_{max}$ .

4.1.2. MOO parameters and objectives

Throughout this example the MOO problem (26) is utilized for obtaining the ABC stencil coefficients. If not stated otherwise, the MOO parameters and objectives are configured as follows:

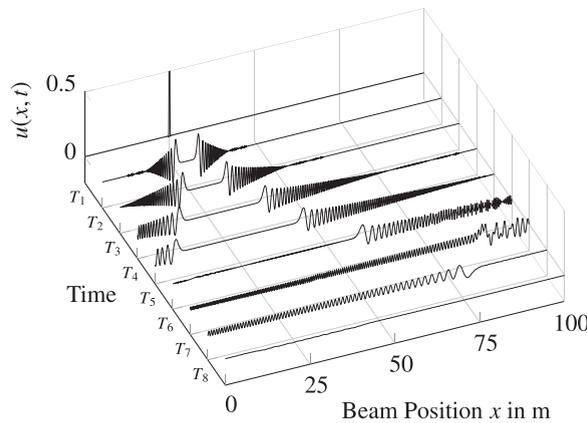


Fig. 5. Displacements  $u(x, t)$  of the pretensioned EBB for selected simulation times.  $x = 0$  m: ABC applied,  $x = 100$  m: clamping BC applied

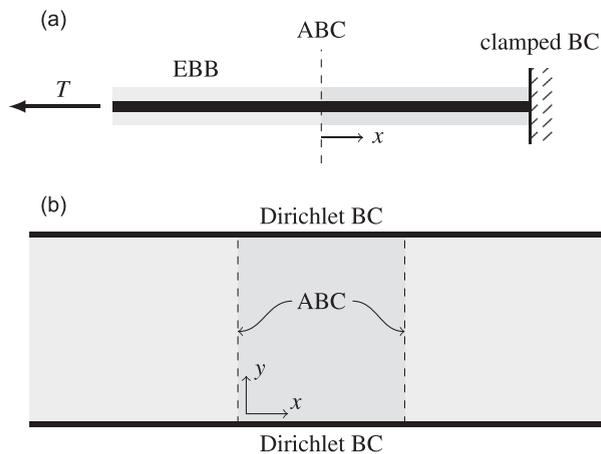


Fig. 6. Elongated reference domains (light gray) and ABC-bounded computational domains (dark gray) for the two examples: (a) EBB under axial load, (b) two-dimensional wave equation.

- The MOO problem is solved by a multi-objective genetic algorithm with a population size of 100 individuals. Thus, the solution represents that of a single objective (best accuracy) optimization problem with a stability constraint (24), however, the MOO treatment allows direct insight into the accuracy/stability-margin trade-off.
- Only the best performing stable solution of the optimized, final solution set is considered.
- The RC (17) and OE (19) accuracy objectives are evaluated at a frequency grid  $\omega_x \in [0, \pi/10\Delta x, 2\pi/10\Delta x, \dots, \pi/\Delta x]$ .
- The stability objective (24) is calculated using a small test system ( $\mathbf{A} \in \mathbb{R}^{10 \times 10}$  of the system (22)).
- The OE accuracy objective (19) is evaluated using  $N_t^{OE} = 5$  and  $N_x^{OE} = 15$  (see Fig. 4).
- Frequency weighting is only considered in Section 4.1.6, in all other sections it is set to  $w(\omega_x) = 1$ .

4.1.3. Quantification of the absorption properties and long-term stability

The absorption properties of the ABCs are quantified by means of the time-dependent approximated error [35]

$$e(t) = \frac{\|\mathbf{u}(t) - \mathbf{u}_{\text{ref}}(t)\|_{[0,L]}}{L} \tag{30}$$

and the approximated global relative space-time error

$$E = \frac{\|\mathbf{u} - \mathbf{u}_{\text{ref}}\|_{[0,L],[0,T_{\text{sim}}]}}{\|\mathbf{u}_{\text{ref}}\|_{[0,L],[0,T_{\text{sim}}]}} \tag{31}$$

Therefore a reference solution  $\mathbf{u}_{\text{ref}}$  – based on the same interior discretization – is computed using a one-sided elongated simulation setup (see Fig. 6a). The elongated setup  $-mL \leq x \leq L$  has clamped boundary condition on both sides. Its elongation factor  $m \in \mathbb{N} \setminus \{0\}$  is chosen such that no reflection of the left boundary enter the truncated simulation domain ( $0 < x < L$ ) during the simulation time  $T_{\text{sim}}$ . The errors (30) and (31) are calculated using the  $L_2$ -norm  $\|\cdot\|_{\mathcal{M}}$  evaluated on the manifold  $\mathcal{M}$ .

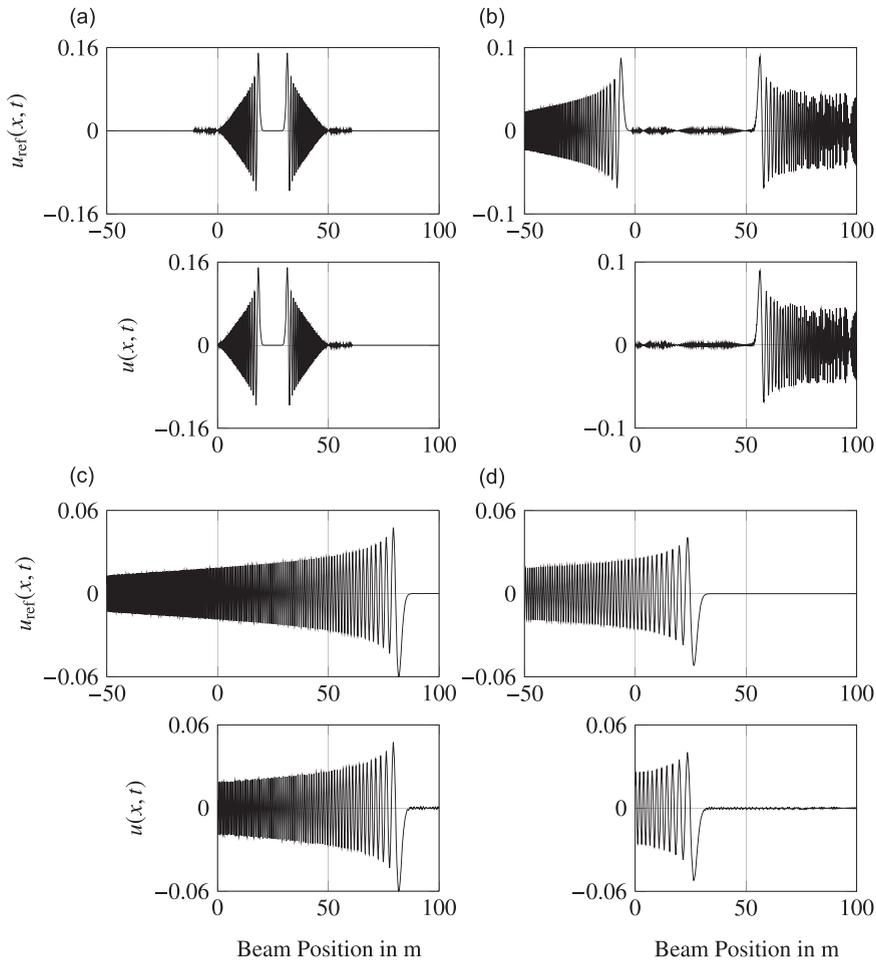


Fig. 7. Comparison of the reference solution  $u_{\text{ref}}(x, t)$  (top) and solution with applied ABCs  $u(x, t)$  (bottom) at: (a)  $t = 0.05$  s, (b)  $t = 0.25$  s, (c)  $t = 0.75$  s and (d)  $t = 1.25$  s.

In comparison to the one-dimensional time-dependent error in Ref. [35], here the error (30) is normalized by  $L$  instead of  $\sqrt{L}$ . This choice renders  $e(t)$  dimensionless.

To verify that the proposed ABCs are stable, long-term simulations will be performed and quantified by the total energy remaining in the system. The total energy remaining in the system is defined as the sum of kinetic energy  $E_{\text{kin}}$  and potential energy  $E_{\text{pot}}$  (see in Ref. [23])

$$E_{\text{tot}}(t) = E_{\text{kin}}(t) + E_{\text{pot}}(t) = \int_0^L \underbrace{(\epsilon_{\text{kin}}(x, t) + \epsilon_{\text{pot}}(x, t))}_{\epsilon_{\text{tot}}(x, t)} dx, \quad (32a)$$

with the total energy per unit length  $\epsilon_{\text{tot}}(x, t)$  and its kinetic and potential contributions

$$\begin{aligned} \epsilon_{\text{kin}}(x, t) &= \frac{1}{2} \rho A \left( \frac{\partial u(x, t)}{\partial t} \right)^2, \\ \epsilon_{\text{pot}}(x, t) &= \frac{1}{2} \left[ T \left( \frac{\partial u(x, t)}{\partial x} \right)^2 + EI \left( \frac{\partial^2 u(x, t)}{\partial x^2} \right)^2 \right]. \end{aligned} \quad (32b)$$

$E_{\text{tot}}(t)$  is computed by approximating the derivatives by central differences and the integration by the trapezoidal rule.

#### 4.1.4. Demonstration of wave absorption

The wave absorption properties of an optimized ABC are demonstrated. The ABC stencil coefficients

$${}_0\mu_0^T = [2.3401 \times 10^{-1} \quad 9.9202 \times 10^{-1} \quad -2.3323 \times 10^{-1} \quad -1.6615 \times 10^{-3}], \quad (33a)$$

$${}_1\mu_0^T = [6.3487 \times 10^{-2} \quad 2.5289 \times 10^{-1} \quad 9.3493 \times 10^{-1} \quad -2.5498 \times 10^{-1}], \quad (33b)$$

are applied on the left boundary ( $x = 0$  m) and were obtained by solving the MOO (26) using the RC accuracy objective (17) and the stability objective (24). The stability margin for the ABC stencil (33) is  $1 - J_{\text{stab}} \approx 9.6769 \times 10^{-5}$  and the accuracy objective value is  $J_{\text{perf,RC}} \approx 8.6661 \times 10^{-2}$ . The clamped BC (28) is applied on the right boundary ( $x = 100$  m).

Fig. 5 visualizes the displacement of the EBB at selected time instances  $T_1 < T_2 < \dots < T_8$ , where the topmost curve depicts the IC (29a).

Time  $T_1$  shows that the initial wavelet has split into two wave packets, traveling leftward and rightward. Additionally, the physical dispersion of the EBB which separates low- and high-frequency content due to differing propagation speeds is clearly visible. Here, high frequency components travel faster than low frequency components. At times  $T_2$ ,  $T_3$  and  $T_4$  the wave packet running leftward towards the ABC at  $x = 0$  m is absorbed while the right wave packet (running towards  $x = 100$  m) disperses further (seen at times  $T_2$ ,  $T_3$ ) and at time  $T_4$  it starts to be totally reflected by the clamping BC (28). At times  $T_5, \dots, T_8$  the total reflection at the right boundary and the subsequent absorption on the left is shown.

A more detailed view is given in Fig. 7, where the solution  $u(x, t)$  with ABCs applied and the reference solution  $u_{\text{ref}}(x, t)$  are shown for selected time instances. Each plot therein consists of the reference solution (top) and the truncated ABC-bounded solution (bottom). It is noted that  $u_{\text{ref}}(x, t)$  has been calculated on a significantly elongated domain  $-1000 \text{ m} \leq x \leq 100 \text{ m}$ , but only  $-50 \text{ m} \leq x \leq 100 \text{ m}$  are shown for clarity. As one can see in Fig. 7, the IC (29a) has a rich

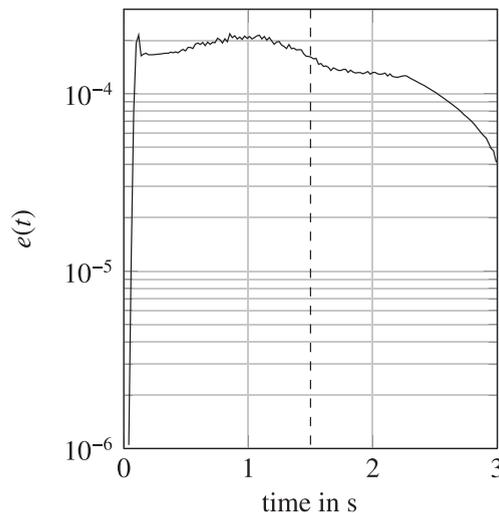


Fig. 8. Time-dependent error  $e(t)$  of the EBB ABC. The dashed line marks the time when the IC has entirely left the truncated domain ( $t = 1.5$  s).

frequency content. However, the agreement of the reference solution and the truncated solution is very good. The time-dependent error  $e(t)$  is given in Fig. 8 and quantifies the degree of absorption. It is initially zero until the leftwards traveling wave packet reaches the boundary at  $x = 0$  m ( $t \approx 0.05$  s). Then, the value of  $e(t)$  stays approximately constant as long as significant signal content remains in the truncated domain ( $0 \text{ m} \leq x \leq 50 \text{ m}$ ). For  $t \geq 1.5$  s the displacement of the reference solution is equal to zero inside the truncated domain (dashed line in Fig. 8) and the error  $e(t)$  decreases again over time.

One important aspect of ABC quality is long-term stability. Ref. [35] reports on the asset of long-term stability. To verify that no such behavior occurs a simulation run of 200 s (two orders of magnitude longer than the time the IC needs to leave the truncated domain in this example) was performed and the total energy  $E_{\text{tot}}(t)$  (32a) was calculated. The result is displayed in Fig. 9, demonstrating that the total energy  $E_{\text{tot}}$  decays and the ABC-bounded system remains stable. Additionally, an eigenvalue analysis for a particular test system is given by the stability condition (Section 3.3) and in the included ABC sensitivity analysis in Section 4.1.7. As all considered, nominal stencils fulfill the stability condition, they yield stable system behavior and are long-term stable.

This simulation example demonstrates that the proposed methodology is capable of producing well-performing and stable ABCs for the EBB. A comparison of the absorption quality RC (17) and the OE (19) performance objective for the optimization of ABCs will be given in the following section.

#### 4.1.5. Comparison of the accuracy objectives

In this section the absorption properties of ABCs resulting from the optimization with respect to the RC accuracy objective (17) and the OE accuracy objective (19) will be compared by means of global relative space–time error (31). Because of the random nature of the genetic algorithm, each run of the MOO leads to a different solution set. To obtain a

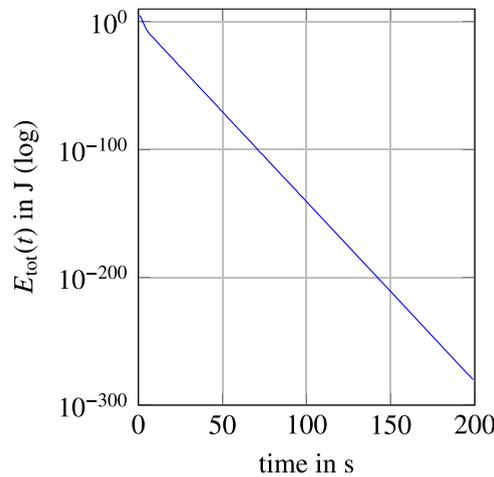


Fig. 9. Long-term energy decay of the optimized ABC for the EBB.

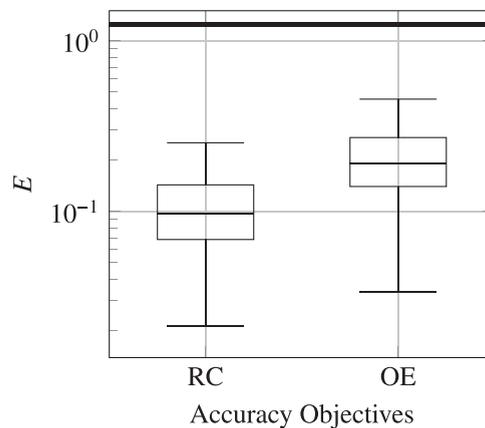


Fig. 10. Box plot comparison for ABCs optimized by the RC (17) (left) and OE (19) (right) accuracy objectives.

statistically relevant statement, 200 optimization runs are carried out. The best stable ABC of each run is applied to the EBB system.

The result is illustrated in Fig. 10 by means of box plots. The horizontal bold line at the top of the plot shows the global relative space–time error for the IC (29a) with clamping BCs at both boundaries ((27) at  $x=0$  and  $x=L$ ). These box plots show that utilizing the RC accuracy objective (17) during optimization yields on average better accuracy than using the OE accuracy objective (19) for  $T_{\text{SIM}} = 1.5$  s. The global relative space–time error  $E$  of the best optimized ABC is 1.72 percent for the RC-optimized and 2.87 percent for the OE-optimized ABCs (relative to the clamped-clamped setup). The average time of solving the MOO problem was slightly larger in the OE case (180.56 s vs. 153.31 s) on a modern office PC (Intel i7).

4.1.6. Frequency weighting

Frequency weighting of the OE accuracy objective (19) and its effect on the optimized ABCs are illustrated. For that purpose, the MOO problem (26) is solved twice using the stability objective (24) and the frequency-weighted OE accuracy objective (19) with the weightings

$$w_{\text{high}}(\omega_x) = \begin{cases} 1 & \omega_x = 0, \dots, \frac{7\pi}{10\Delta x} \\ 5000 & \omega_x = \frac{8\pi}{10\Delta x}, \dots, \frac{\pi}{\Delta x} \end{cases} \quad (34a)$$

and

$$w_{\text{low}}(\omega_x) = \begin{cases} 5000, & \omega_x = 0, \dots, \frac{2\pi}{10\Delta x} \\ 1 & \omega_x = \frac{8\pi}{10\Delta x}, \dots, \frac{\pi}{\Delta x} \end{cases} \quad (34b)$$

for high and low frequency weighting, respectively.

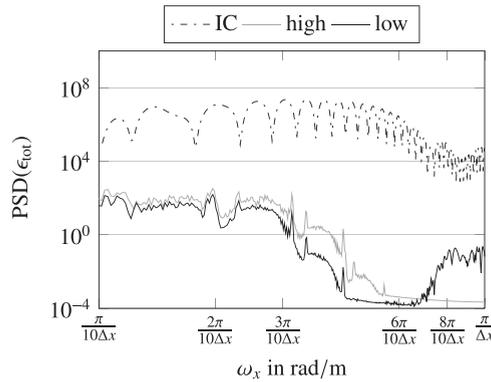


Fig. 11. Power spectral density of  $\epsilon_{\text{tot}}$  (32a) for the IC and residual signal after absorption through the high- and low-frequency-weighted ABCs, respectively.

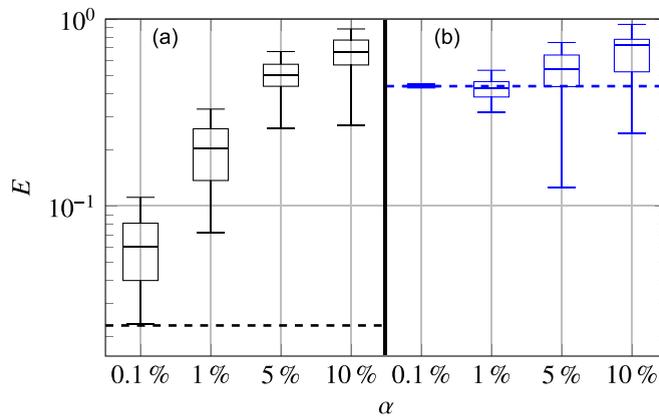


Fig. 12. Evaluation of ABC stencils with (a)  $J_{\text{perf}} = 8.6661 \times 10^{-2}$  and  $J_{\text{stab}} = 9.9990 \times 10^{-1}$  (black), b)  $J_{\text{perf}} = 1.1528 \times 10^{-1}$  and  $1 - J_{\text{stab}} = 5.3909 \times 10^{-2}$  (blue). (For interpretation of the references to color in this figure caption, the reader is referred to the web version of this paper.)

The results are displayed in Fig. 11 in terms of the power spectral density (PSD) of the total energy per unit length  $\epsilon_{\text{tot}}(x, t)$  (32a) of the EBB (obtained by Welch's method [42]). The PSD of the IC  $\epsilon_{\text{tot}}(x, 0)$  and  $\epsilon_{\text{tot}}(x, T)$  for the solution of the high- and low-frequency-weighted ABC cases ('high' and 'low') are shown.

As expected, the frequency weighting (34) used in the optimization influences the absorption properties of the ABCs such that the residual frequency content has smaller magnitudes at the low and high frequencies for the weightings  $w_{\text{low}}$  and  $w_{\text{high}}$ , respectively.

4.1.7. Sensitivity analysis of the ABC stencil

The sensitivity analysis of the ABC stencil (33) will be performed by considering stability (eigenvalue analysis) and accuracy (approximated global relative space–time error (31) and the setup from Section 4.1.1). For that each stencil value is relatively and randomly varied by  $\alpha = \pm 0.1$  percent,  $\alpha = \pm 1$  percent,  $\alpha = \pm 5$  percent and  $\alpha = \pm 10$  percent, where  $\alpha$  is the perturbation level. Additionally, a second ABC stencil

$${}_0\mu_0^T = [2.3417 \times 10^{-1} \quad 9.6807 \times 10^{-1} \quad -1.8969 \times 10^{-1} \quad -5.1449 \times 10^{-3}], \tag{35a}$$

$${}_1\mu_0^T = [6.3472 \times 10^{-2} \quad 2.6482 \times 10^{-1} \quad 9.0721 \times 10^{-1} \quad -2.5508 \times 10^{-1}], \tag{35b}$$

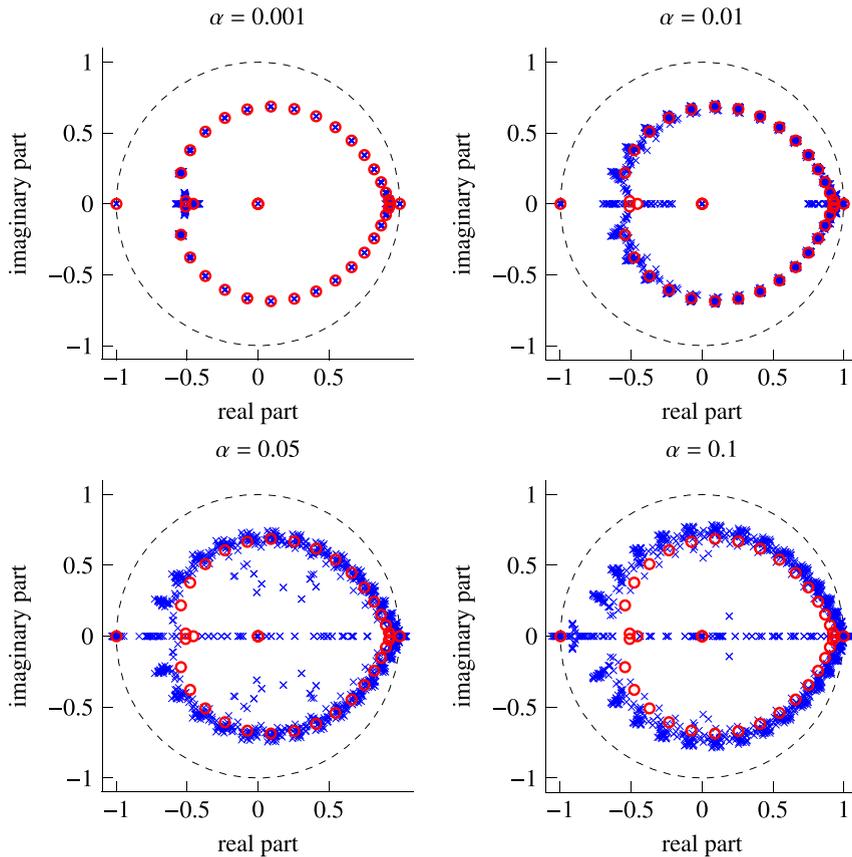
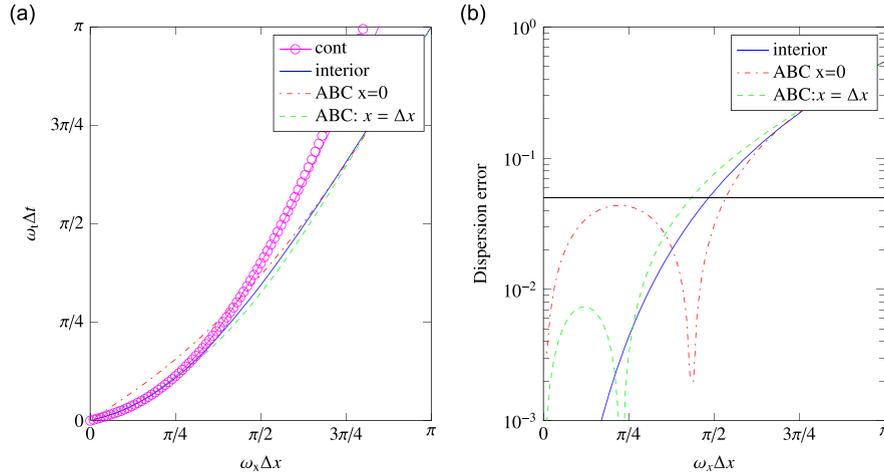


Fig. 13. Eigenvalue distribution of a small ( $N_x=20$ ) test setup. The eigenvalues of the nominal stencil ( $\circ$ ) and the perturbed stencils ( $\times$ ).

Table 1  
Number of unstable ABCs for different perturbation levels  $\alpha$ .

| $\alpha$ | $\pm 0.1\%$ | $\pm 1\%$ | $\pm 5\%$ | $\pm 10\%$ |
|----------|-------------|-----------|-----------|------------|
| ABC (33) | 24          | 35        | 28        | 29         |
| ABC (35) | 0           | 0         | 12        | 19         |



**Fig. 14.** (a) Dispersion relation of the continuous PDE, using interior stencil (blue solid) and using the ABC stencils (red dashed dotted at  $x=0$  and green dashed at  $x = \Delta x$ ). (b) Dispersion error in logarithmic scale. (For interpretation of the references to color in this figure caption, the reader is referred to the web version of this paper.)

with the stability margin  $1 - J_{\text{stab}} \approx 5.3909 \times 10^{-2}$  and accuracy objective value is  $J_{\text{perf,RC}} \approx 1.1528 \times 10^{-1}$  is considered. This stencil has a larger stability margin and reflection coefficient and is thus excepted to be more robust concerning stability, but less accurate.

Starting with the accuracy for each perturbation level  $N_{\text{perturb}} = 50$  perturbations were applied to the nominal stencils (33) and (35). Taking only stable perturbed stencils into account, the errors are displayed by means of box plots in Fig. 12. The results are displayed the in (a) and (b) for the ABCs stencils (33) and (35), respectively. The bold dashed horizontal lines in both figures mark the errors of the nominal ABC stencils. As expected, the stencil (33) is more accurate and perturbations lead to an increase of the error. The perturbation of stencil (35) leads for small perturbations ( $\pm 0.1$  percent) to no significant change in accuracy. Increasing the perturbation level the median of the error increases, but some stable stencils outperform the nominal stencil (35).

For the sensitivity analysis of the stability the eigenvalue distribution for the same  $N_{\text{perturb}} = 50$  stencils of the ABC stencil (33) is considered (see Fig. 13). In this figure the nominal eigenvalues are marked by circles ( $\circ$ ) and those of the perturbed ABC stencil eigenvalue are marked by crosses ( $\times$ ). The number of perturbed unstable ABCs is quantified in Table 1 for both ABC stencils. Summarizing the result, one can see that the increase of the perturbation level  $\alpha$  leads to a stronger deviation of the eigenvalues and also to more eigenvalues outside the unit circle (see Fig. 13). However, because of the larger stability margin the ABC stencil (35) is more robust and all ABCs are stable for  $\alpha = \pm 0.1$  percent and  $\alpha = \pm 1$  percent. Then the number of unstable ABCs increases. In contrast, the number of unstable ABCs for (33) is typically above 50 percent.

The eigenvalue distribution of the ABC stencil (35) is omitted here, because it yields qualitatively similar results. The major differences have been summarized in Table 1.

#### 4.1.8. Comparison of the continuous and discrete dispersion relation

In comparison to literature (e.g. Refs. [34,33,43]), where the dispersion relation (DR) is considered for a specific stencil (space and time discretization separately), here the DR of the entire PDE is considered as used in Ref. [6]. The dispersion relation of the continuous EBB (1) is calculated as

$$\rho A \omega_t^2 = \omega_x^4 EI + \omega_x^2 T. \quad (36)$$

The considered DRs are displayed in Fig. 14(a). One can clearly see that for the interior and ABCs at  $x=0$  stencils are in good agreement with the continuous DR up to  $\omega_x \Delta x \approx \pi/2$ . For high frequencies all discrete DRs diverge similarly from the continuous DR. To compare the ABC and interior stencils quantitatively for a chosen error level  $E_{\text{DISP}}$  typically the quantity Points-per-Wavelength (PPW) is used (see Refs. [43,44]). Here, a reasonable choice is  $E_{\text{DISP}} = 5$  percent (the bold horizontal line in Fig. 14(b)) leading to 4.13, 3.74 and 4.61 PPWs for the interior, the ABC at  $x=0$  and the ABC at  $x = \Delta x$ , respectively. In Refs. [43] and [44], 7 and between 3.36 and 4.22 PPWs were achieved for high-order stencils approximating the first derivative  $\partial/\partial x$  using  $E_{\text{DISP}} = 0.3$  percent with  $N_x^{\text{INT}} = 7$  and  $E_{\text{DISP}} = 0.5$  percent with  $N_x^{\text{INT}} = 9 \dots 13$ , respectively.

#### 4.2. ABCs for the two-dimensional wave equation

The scalar two-dimensional wave equation is given by [38]

$$\frac{\partial^2 u}{\partial t^2} = c^2 \left( \frac{\partial^2 u}{\partial x^2} + \frac{\partial^2 u}{\partial y^2} \right), \quad (37)$$

with the vertical displacement  $u(x, y, t)$ , the wave propagation speed  $c$  and two spatial variables  $x$  and  $y$ . Here it is assumed that the PDE models small-amplitude waves in a membrane, and for the following numerical results the physical parameters were arbitrarily chosen as

$$\rho = 1 \text{ kg/m}^2, \quad f = 100 \text{ N/m}, \quad c = \sqrt{f/\rho} = 10 \text{ m/s}, \quad (38)$$

where  $c$  is the wave propagation speed,  $f$  is the tensile line load (force per unit length) applied at the boundary of the membrane and  $\rho$  is the area density of the membrane material.

##### 4.2.1. Implementation for the two-dimensional wave equation

Some modifications to the methods described in Sections 2 and 3 have to be made to investigate higher-dimensional problems. They will be sketched for the case of the two-dimensional wave equation (37).

The FD approximation of partial derivatives with respect to  $y$  is obtained analogously to (2) for an evenly spaced grid  $y = [0, \Delta y, \dots, N_y \Delta y]$  with  $\Delta y \in \mathbb{R}^+$  and  $N_y \in \mathbb{N}$ . The generic stencil (3) now contains an additional sum in the  $y$ -direction

$$u_{k,m}^{n+1} = \sum_{i=0}^{N_x^{\text{INT}}-1} \sum_{j=-(N_x^{\text{INT}}-1)/2}^{(N_x^{\text{INT}}-1)/2} \sum_{p=-(N_y^{\text{INT}}-1)/2}^{(N_y^{\text{INT}}-1)/2} a_{j,p}^i u_{k+i,j,m+p}^{n-i}, \quad (39)$$

and the boundary stencils are modified analogously. Using central differences on the two-dimensional wave equation (37) leads to  $N_x^{\text{INT}} = N_y^{\text{INT}} = 3$  and  $N_t^{\text{INT}} = 2$ . The harmonic wave solution is extended in the  $y$ -direction:

$$u_{k,m}^n = (e^{i\omega_x \Delta x})^k (e^{i\omega_y \Delta y})^m (e^{i\omega_t \Delta t})^n = \kappa^k \zeta^m \tau^n. \quad (40)$$

Consequently, a second spatial wave number,  $\omega_y$ , arises and the dispersion relation now connects  $\omega_x$ ,  $\omega_y$ , and  $\omega_t$ . Additionally, the angle  $\varphi = \varphi(\omega_x, \omega_y)$  describes the traveling direction of the wave and the dispersion relation can be parametrized in  $\varphi$  and  $\omega_t$ .

The necessary adoptions to the objective functions will be demonstrated on the OE accuracy objective (19) and the stability objective (24). The output-error (18) for the two-dimensional wave equation is

$$e_{\text{OE}}(\varphi, \omega_t) = \sum_{n=2}^{N_t^{\text{OE}}} \sum_{k=1}^{N_x^{\text{OE}}} \sum_{m=1}^{N_y^{\text{OE}}} \left| u_{k,m}^n - \kappa^k \zeta^m \tau^n \right|^2, \quad (41)$$

and the objective function is obtained by aggregating this error function over the parameters  $\varphi$  and  $\omega_t$ :

$$J_{\text{perf,OE}} = \int_0^{\pi/2} \int_0^{\pi/\Delta x} w(\omega_t, \varphi) e_{\text{OE}}(\omega_t, \varphi) d\omega_t d\varphi. \quad (42)$$

To evaluate the stability objective (24) the state-space representation of a test system needs to be constructed. The  $N_x \times N_y$

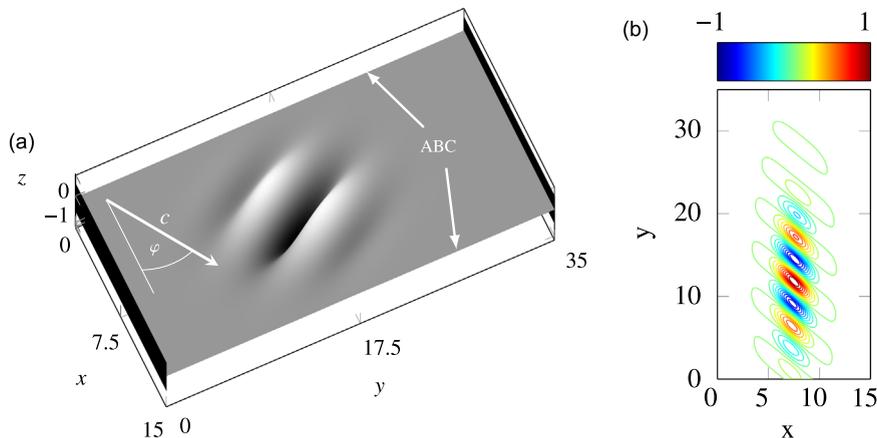


**Fig. 15.** (a) Problem setup for the two-dimensional wave example. ABCs are applied at  $x = 0$  m and  $x = 15$  m. At  $y = 0$  m and  $y = 35$  m Dirichlet BCs are applied. (b) Problem setup as contour plot.

solution values at each relevant time instant have to be organized as a stacked augmented state vector  $\mathbf{v} \in \mathbb{R}^N$ , with  $N = (N_t^{\text{up}} - 1)N_x N_y$ , leading to a system matrix  $\mathbf{A} \in \mathbb{R}^{N \times N}$ .

4.2.2. Available absorbing boundary conditions

The optimized ABC stencils will be compared to already available ABCs from the literature. In 1977, Engquist and Majda [3] developed a method for obtaining absorbing boundary conditions of arbitrary order for the wave equation. However, the original Engquist–Majda boundary conditions are of practical use only in low-order because of their rapid increase in algebraic complexity for high-order formulations [11]. Here, the second-order Engquist–Majda (EM2) boundary conditions are applied:

$$\frac{\partial^2 u}{\partial x \partial t} - \frac{\partial^2 u}{\partial t^2} + \frac{1}{2} \frac{\partial^2 u}{\partial y^2} = 0, \tag{43}$$

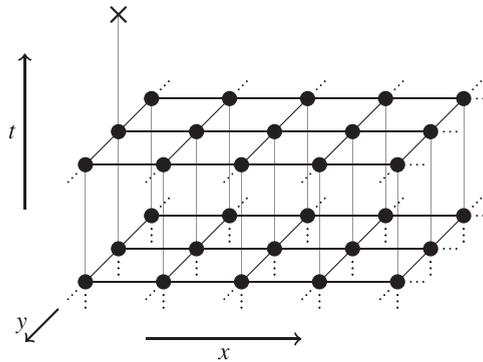


Fig. 16. Sketch of the (5,3,2) ABC stencil structure.

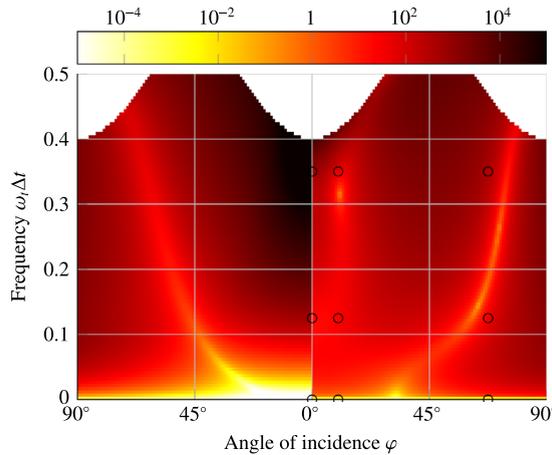


Fig. 17. Log-scaled output error  $e_{\text{OE}}(\varphi, \omega_t)$  (41) as a function of the angle of incidence  $\varphi$  and the frequency  $\omega_t \Delta t$  for the second-order Engquist–Majda ABC (left) and an optimized (3,3,2) ABC stencil (right). The optimization grid used for obtaining the latter is marked by  $\circ$ .

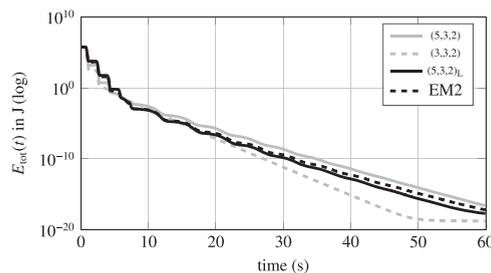


Fig. 18. Long-term energy decay of the optimized ABCs with high-frequency waves ( $\omega_t \Delta t = 0.325$ ) for the two-dimensional wave equation.

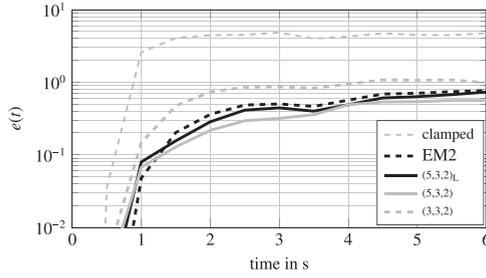


Fig. 19. Total error  $e(t)$  for different ABCs with low-frequency waves ( $\omega_t \Delta t = 0.035$ ), arriving with an angle of incidence of  $\varphi = 45^\circ$ .

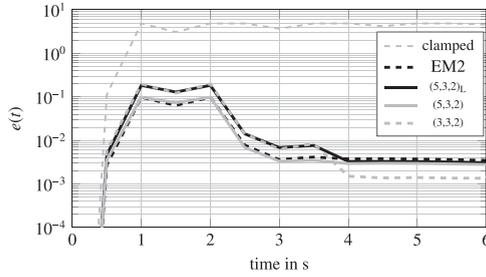


Fig. 20. Total error  $e(t)$  for different ABCs with mid-frequency waves ( $\omega_t \Delta t = 0.15$ ), arriving with an angle of incidence of  $\varphi = 5^\circ$ .

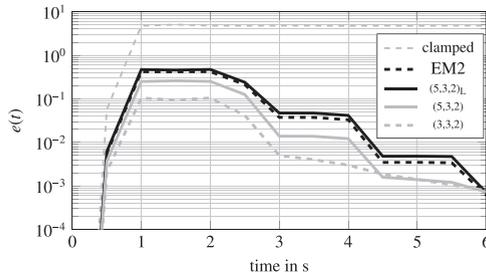


Fig. 21. Total error  $e(t)$  for different ABCs with high-frequency waves ( $\omega_t \Delta t = 0.325$ ), arriving with an angle of incidence of  $\varphi = 10^\circ$ .

where  $x$  and  $y$  denote the directions in normal and tangential direction on the boundary, respectively. In this work, all derivatives in (43) were discretized using second-order-accurate finite difference schemes.

Another important ABC for wave problems is the Higdon ABC [30]:

$$\prod_{j=1}^J \left( \frac{\partial u(x, y, t)}{\partial t} + C_j \frac{\partial u(x, y, t)}{\partial x} \right) = 0, \quad (44)$$

with constants  $C_j$  and  $J$  denoting the order of the ABC. Higdon proved that every ABC that is based on a symmetric rational approximation of the dispersion relation (for outgoing waves) is either equivalent to (44) or not optimal [30]. Moreover, for  $J=2$  and certain values of  $C_j$ , the Higdon ABC corresponds to the EM2 ABC (43). Theoretically, the same problems with higher derivatives as for the Engquist–Majda ABCs arises when implementing (44). However, several different methods exist for efficiently applying the Higdon ABCs; see [12] for a corresponding review.

#### 4.2.3. Problem setup

Fig. 15(a) exemplarily shows the simulation setup with a very-low-frequency wave packet that is started with an initial velocity of  $c$  in the direction associated with angle  $\varphi$ . In Fig. 15(b) the simulation setup is displayed as a contour plot (compare Appendix B). The initial condition for all simulation runs was chosen as

$$u_{k,m}^0 = \text{Re} \left( e^{i\omega_x \Delta x k} e^{i\omega_y \Delta y m} \right) e^{-0.4(k\Delta x - x_c)^2} e^{-0.015(m\Delta y - y_c)^2}, \quad (45)$$

with appropriately selected centers  $x_c$  and  $y_c$ . The domain size was chosen as  $l_x = 15$  m,  $l_y = 35$  m, and the ABCs are applied at  $x = 0$  m and  $x = 15$  m while the remaining two boundaries are fixed (Dirichlet BCs). The step sizes were chosen as  $\Delta x = \Delta y = 0.05$  m and  $\Delta t = 0.001$  s.

#### 4.2.4. Optimization setup

Throughout the following examples the OE accuracy objective (42) is utilized to quantify the absorption properties. The stability condition (24) has been evaluated for a test system of size  $N_x = N_y = 7$ , which leads to a system matrix  $\mathbf{A} \in \mathbb{R}^{98 \times 98}$ , see (22). However, by eliminating zero-states that result from Dirichlet BCs the system matrix is reduced to  $\mathbf{A} \in \mathbb{R}^{60 \times 60}$ .

Especially for larger ABC stencil sizes (due to the large number of decision variables), it was observed that convergence of the MOO genetic algorithm to the actual Pareto front may be difficult to achieve. Throughout this example, only single-objective optimization problems were formulated and solved by a *pattern-search* method [27], where the accuracy objective was multiplied with a large penalty term when the stability objective (24) indicated instability, which corresponds to using a stability constraint (24).

#### 4.2.5. Investigated stencil configurations

The structure of the studied ABC realizations is denoted here by the triplet  $(N_x^{ABC}, N_y^{ABC}, N_t^{ABC})$ , where  $N_x^{ABC}$  and  $N_y^{ABC}$  are the spatial widths in normal and tangential direction, respectively (for the ABC along the  $x = 0$  m edge), and  $N_t^{ABC}$  is the number of time instants that are needed for the computation of the next boundary grid point. Fig. 16 shows the structure of a (5,3,2) stencil where the grid points marked by dots ( $\bullet$ ) are needed for the computation of the future boundary grid point marked by a cross ( $\times$ ).

The following ABCs are further investigated: an EM2 ABC [3] and proposed ABCs of structures (3,3,2), (5,3,2), and (5,3,2)<sub>L</sub>, where the latter is only optimized for low frequencies. Their numerical values are summarized in Appendix A.

For discretizing the EM2 ABC second-order accuracy approximations were used, yielding a (4,3,2) stencil. The (3,3,2) ABC is optimized over a grid  $\varphi \times \omega_t \Delta t = [0^\circ, 10^\circ, 67.5^\circ] \times [0 \text{ rad}, 0.125 \text{ rad}, 0.35 \text{ rad}]$  with a focus on higher frequencies. The (5,3,2) ABC is optimized to obtain an overall well-performing ABC, independent of the angle  $\varphi$  and frequency  $\omega_t$  of the incoming wave.

#### 4.2.6. ABC comparison by output-error accuracy

The ABC with the structure (3,3,2) is compared to the second-order Engquist–Majda (EM2) ABC [3]. In Fig. 17, the values of the output error function (41) are plotted for a fine grid over  $\varphi$  and  $\omega_t \Delta t$ . Dark regions indicate a large error, whereas the bright regions correspond to small errors. As can be seen in Fig. 17, the EM2 ABC performs very well in the low-frequency range, while the error made at high-frequency waves arriving in normal direction is very large. However, the EM2 needs a larger stencil (4,3,2) than the optimized (3,3,2) ABC. The optimized (3,3,2) ABC already leads to good overall performance in this configuration. It is noted that for plotting the minimum of the output error function was clipped to  $5 \times 10^{-4}$  to obtain a better scaling in the very-low-frequency range.

#### 4.2.7. True error comparison and long-term stability

In the following, all ABC stencils introduced in Section 4.2.5 are compared. For the quantification of the absorption properties the time-dependent error in analogy to (30) is defined for the two-dimensional case

$$e(t) = \frac{\|\mathbf{u}(t) - \mathbf{u}_{\text{ref}}(t)\|_{[0, l_x] \times [0, l_y]}}{\sqrt{A}} \quad (46)$$

where  $A = l_x l_y$  is the computational area and  $\mathbf{u}_{\text{ref}}$  is the reference solution computed on a much larger domain ( $-40 \text{ m} \leq x \leq +40 \text{ m}$ ), see Fig. 6(b). The verification of the long-term stability is carried out by evaluating the total energy remaining inside the computational domain  $x \in [0, l_x]$ ,  $y \in [0, l_y]$  [23]:

$$E_{\text{tot}}(t) = E_{\text{kin}}(t) + E_{\text{pot}}(t), \quad (47a)$$

$$E_{\text{kin}}(t) = \frac{\rho}{2} \int_0^{l_x} \int_0^{l_y} \left( \frac{\partial u}{\partial t} \right)^2 dy dx, \quad (47b)$$

$$E_{\text{pot}}(t) = \frac{f}{2} \int_0^{l_x} \int_0^{l_y} \left[ \left( \frac{\partial u}{\partial x} \right)^2 + \left( \frac{\partial u}{\partial y} \right)^2 \right] dy dx. \quad (47c)$$

Long-term simulations of the test system with the obtained ABCs in place showed that they indeed did not render the finite-difference scheme unstable (see Fig. 18).

The results by means of time-dependent error  $e(t)$  are plotted in the Figs. 19–21 for different angles and frequencies of the initial waves. Similar to the EBB example the time-dependent error  $e(t)$  stays zero until the wave packets reach the boundary and stays then approximately constant. The time-domain plots are displayed in Figs. B1–B3.

These results confirm that the accuracy of the optimized ABCs compares favorably over a wide frequency range with the EM2 ABC, whose stencil is essentially of the same size as those used for the optimized ABCs. Additionally, the flexibility and tunability of the optimization-based approach provides significant design advantages in practice.

## 5. Conclusion and discussion

A generic method to produce well-performing and stable absorbing boundary conditions (ABCs) for finite-difference approximations of partial differential equations with wave propagation effects has been proposed. The ABC stencil coefficients are utilized as decision variables in an optimization problem in which both absorption accuracy and stability are considered. This approach requires only modest analytical treatment of the underlying partial differential equations and provides great flexibility to tune specific properties of the resulting ABCs.

The versatility of the proposed method is demonstrated at two applications – the Euler–Bernoulli bending beam under axial load (for which no ABCs are yet known) and the two-dimensional wave equation. The proposed accuracy objectives are compared and discussed for the Euler–Bernoulli beam example, well-performing ABCs are obtained, and the effect of a frequency-weighted accuracy formulation is investigated. The ABC optimization method is also applied for the well-known two-dimensional scalar wave problem, and it produces highly absorbing BCs, equivalent in accuracy to those derived by Engquist and Majda [3] analytically. Moreover, the behavior of the optimized ABCs can be directly tuned with respect to frequency and angle-of-incidence which provides a large degree of flexibility.

The numeric approach to obtain high-accuracy ABCs is a powerful complementary approach to the analytic derivation of ABCs. The optimization method can simply be transferred to different types of problems and it is straightforward to tune the ABC's frequency or directional behavior. As a result, well-performing ABCs could become available for a wide class of distributed-parameter problems addressed by the finite-difference method.

In future research work, the presented method to obtain ABCs will be tested on complex boundary geometries (e.g. corners) and on other types of equations (such as the wave equation in moving coordinates). The method could also be extended to linearized Euler equation which is governed by a set of three coupled PDEs leading to three coupled dispersion relations. This requires a careful investigation of this PDE and its dispersion relation, to verify if all necessary assumptions for the proposed method are fulfilled.

## Acknowledgment

This work has partially been financed by the Austrian Research Promotion Agency (FFG) under Grant nos. 836449 and 841331.

## Appendix A. ABC stencil values two-dimensional wave equation

The ABC stencil coefficient values  ${}_{(x,y)}\mu_t^T$  are defined in analogy to the one-dimensional stencil (see Section 2). Numbers are given with power-10 exponential notation e.g.  $1.2 \times 10^{-1} = 1.2e-1$ .

For the (3,3,2) stencil one obtains

$$\begin{aligned} {}_{(x,0)}\mu_0^T &= [1.80717 \times 10^{-1} \quad 1.09193e+00 \quad 1.82365 \times 10^{-1}] \\ {}_{(x,1)}\mu_0^T = {}_{(x,-1)}\mu_0^T &= [-1.81047 \times 10^{-1} \quad -6.89779 \times 10^{-2} \quad 3.37948 \times 10^{-1}] \\ {}_{(x,0)}\mu_1^T &= [-6.99544 \times 10^{-2} \quad -4.32682 \times 10^{-1} \quad -1.72127 \times 10^{-1}] \\ {}_{(x,1)}\mu_1^T = {}_{(x,-1)}\mu_1^T &= [3.60531 \times 10^{-1} \quad -6.56820 \times 10^{-2} \quad -1.49357 \times 10^{-1}] \end{aligned}$$

with  $x = 0, \dots, 2$ . The (5,3,2) and (5,3,2)<sub>L</sub> are defined as

$$\begin{aligned} {}_{(x,0)}\mu_0^T &= [1.70526 \times 10^{-2} \quad 1.71110e+00 \quad 7.25865 \times 10^{-3} \quad 3.20594 \times 10^{-1} \quad 2.62183 \times 10^{-3}] \\ {}_{(x,1)}\mu_0^T = {}_{(x,-1)}\mu_0^T &= [-8.52673 \times 10^{-2} \quad -3.38745 \times 10^{-4} \quad -1.69488 \times 10^{-3} \quad -3.23486 \times 10^{-4} \quad 1.64642 \times 10^{-3}] \\ {}_{(x,0)}\mu_1^T &= [-3.38745 \times 10^{-4} \quad -7.39300 \times 10^{-1} \quad -3.38745 \times 10^{-4} \quad -3.47995 \times 10^{-1} \quad 1.79749 \times 10^{-3}] \\ {}_{(x,1)}\mu_1^T = {}_{(x,-1)}\mu_1^T &= [8.78247 \times 10^{-2} \quad -3.38745 \times 10^{-4} \quad -1.69373 \times 10^{-4} \quad -3.38745 \times 10^{-4} \quad -1.69373 \times 10^{-4}] \end{aligned}$$

and

$$\begin{aligned} {}_{(x,0)}\mu_0^T &= [1.74426 \times 10^{-2} \quad 1.71133e+00 \quad 7.00779 \times 10^{-3} \quad 3.18287 \times 10^{-1} \quad -1.68786 \times 10^{-3}] \\ {}_{(x,1)}\mu_0^T = {}_{(x,-1)}\mu_0^T &= [-7.35061 \times 10^{-2} \quad 5.12695 \times 10^{-5} \quad -1.71350 \times 10^{-3} \quad 5.12695 \times 10^{-5} \quad 2.56348 \times 10^{-5}] \\ {}_{(x,0)}\mu_1^T &= [5.12695 \times 10^{-5} \quad -7.39105 \times 10^{-1} \quad 5.12695 \times 10^{-5} \quad -3.47800 \times 10^{-1} \quad 1.07361 \times 10^{-3}] \end{aligned}$$

$${}_{(x,1)}\mu_1^T = {}_{(x,-1)}\mu_1^T = \left[ 8.41440 \times 10^{-2} \quad 5.12695 \times 10^{-5} \quad 2.56348 \times 10^{-5} \quad 5.12695 \times 10^{-5} \quad 2.56348 \times 10^{-5} \right]$$

with  $x = 0, \dots, 4$ , respectively.

**Appendix B. Time domain solutions of the two-dimensional wave equation**

The following Figs. B1–B3 show the time domain results for the  $(5,3,2)_L$ ,  $(5,3,2)$ ,  $(3,3,2)$  stencils for low, mid and high frequency ICs, respectively. The ABC results (middle columns) are compared with the reference solution (left columns) and EM2 result (right columns) at different time instances.

Fig. B1 shows that both ABCs perform well for low frequencies. The third row of this figure shows that there are small differences in the middle ( $5 < x < 10, 10 < y < 20$ ) and the upper-right ( $10 < x < 15, 20 < y < 30$ ) part of the computational domain. The mid frequency solution in Fig. B2 shows again nearly perfect results at  $t = 0.75$  s for the ABCs. At  $t = 1$  s the

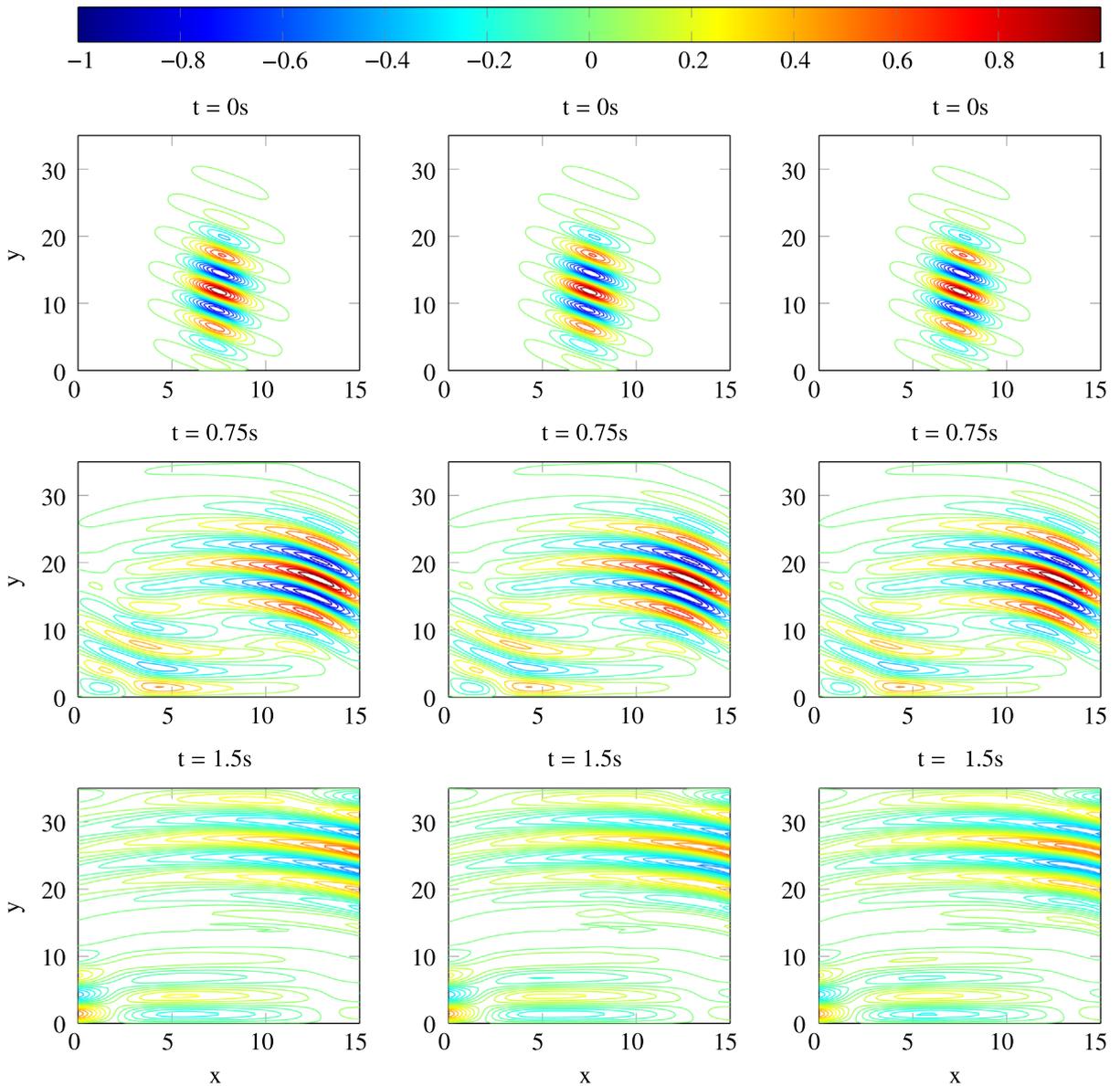


**Fig. B1.** Time domain solution for the low frequency IC and the  $(5,3,2)_L$  stencil: reference solution (left), ABC solution (mid) and EM2 (right).

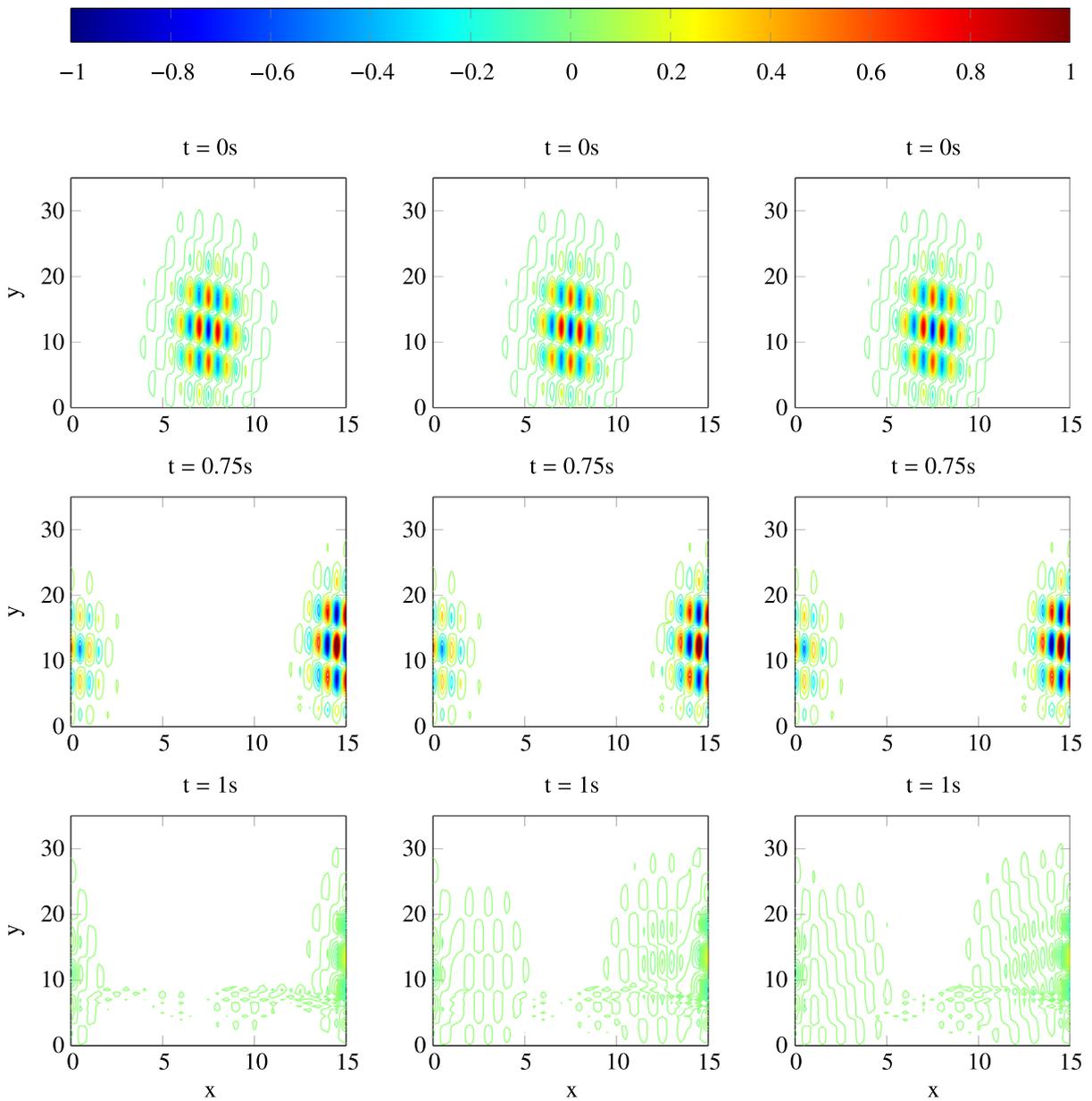


**Fig. B2.** Time domain solution for the mid frequency IC and the (5,3,2) stencil: reference solution (left), ABC solution (mid) and EM2 (right).

(5,3,2)-stencil reflects more than in the low frequency case, because the ABC is not optimized for mid frequencies. In this case the (5,3,2) and EM2 solution perform equally well. In Fig. B3 one can clearly see that the (3,3,2)-stencil absorbs the greater part of incoming waves and achieves a better result than EM2.

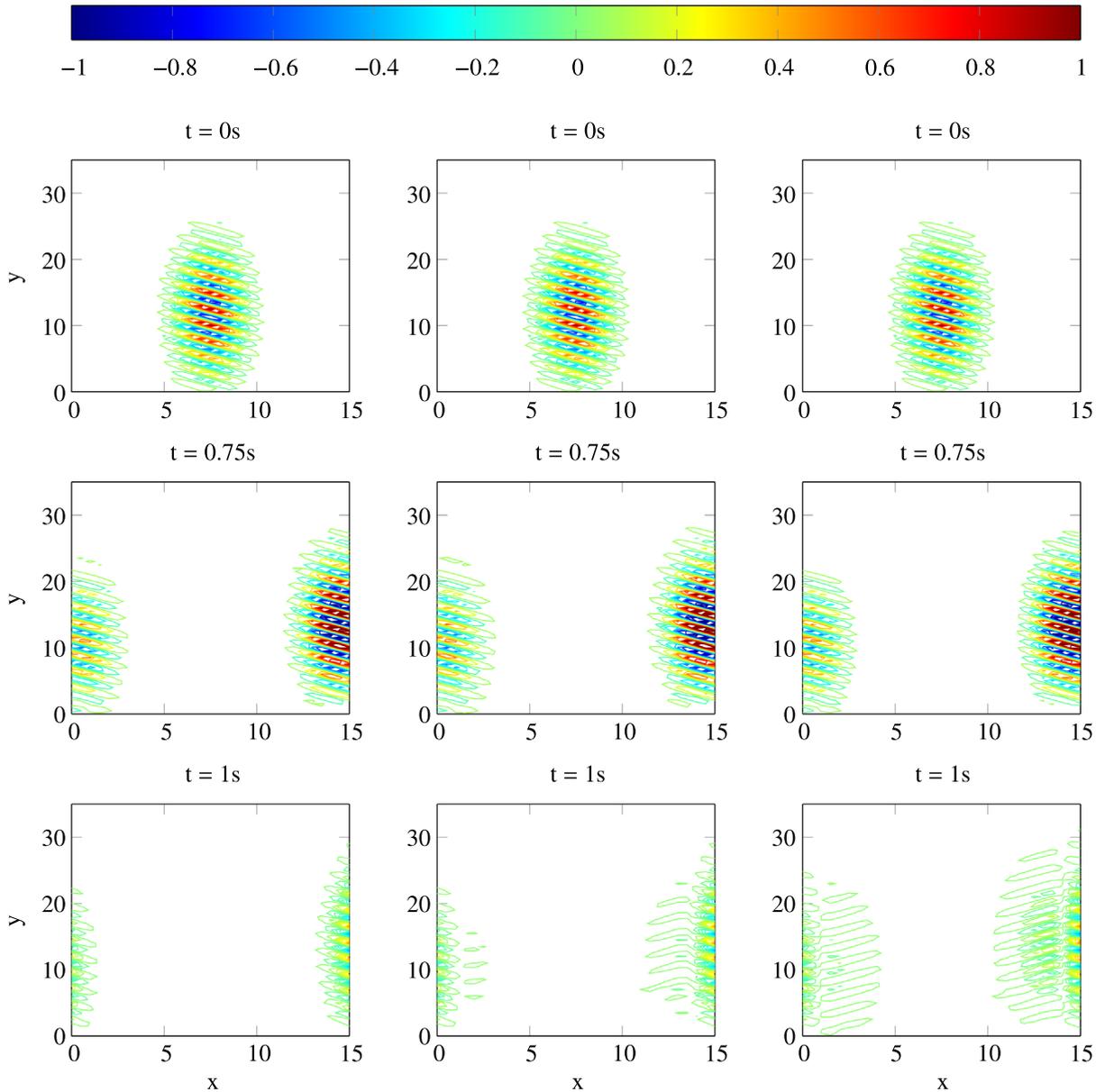


**Fig. B3.** Time domain solution for the high frequency IC and the (3,3,2) stencil: reference solution (left), ABC solution (mid) and EM2 (right).

### Appendix C. Supplementary data

Supplementary data associated with this paper can be found in the online version at <http://dx.doi.org/10.1016/j.jsv.2015.12.006>.

### References

- [1] A. Sommerfeld, *Partial Differential Equations in Physics, Pure and Applied Mathematics*, Elsevier Science, New York, 1949.
- [2] J. Strikwerda, *Finite Difference Schemes and Partial Differential Equations*, Wadsworth Publ. Co., Belmont, CA, USA, 1989.
- [3] B. Engquist, A. Majda, Absorbing boundary conditions for numerical simulation of waves, *Proceedings of the National Academy of Sciences* 74 (5) (1977) 1765–1766.
- [4] A. Bayliss, E. Turkel, Radiation boundary conditions for wave-like equations, *Communications on Pure and Applied Mathematics* 33 (6) (1980) 707–725.
- [5] I. Shevchenko, M. Kaltenbacher, B. Wohlmuth, Absorbing boundary conditions for a wave equation with a temperature-dependent speed of sound, *Journal of Computational Acoustics* 21 (2) .

- [6] R. Higdon, Absorbing boundary conditions for difference approximations to the multi-dimensional wave equation, *Mathematics of Computation* 47 (176) (1986) 437–459.
- [7] R. Higdon, Radiation boundary conditions for elastic wave propagation, *SIAM Journal of Numerical Analysis* 27 (4) (1990) 831–869.
- [8] R. Higdon, Radiation boundary conditions for dispersive waves, *SIAM Journal of Numerical Analysis* 31 (1) (1994) 64–100.
- [9] T. Hagstrom, A. Mar-Or, D. Givoli, High-order local absorbing conditions for the wave equation: extensions and improvements, *Journal of Computational Physics* 227 (6) (2008) 3322–3357.
- [10] D. Givoli, B. Neta, High-order non-reflecting boundary scheme for time-dependent waves, *Journal of Computational Physics* 186 (1) (2003) 24–46.
- [11] D. Givoli, B. Neta, High-order non-reflecting boundary conditions for dispersive waves, *Wave Motion* 37 (3) (2003) 257–271.
- [12] D. Givoli, High-order local non-reflecting boundary conditions: a review, *Wave Motion* 39 (4) (2004) 319–326.
- [13] M. Israeli, S.A. Orszag, Approximation of radiation boundary conditions, *Journal of Computational Physics* 41 (1) (1981) 115–135.
- [14] A. Mimani, Z. Prime, C. Doolan, P. Medwell, A sponge-layer damping technique for aeroacoustic time-reversal, *Journal of Sound and Vibration* 342 (2015) 124–151.
- [15] J.-P. Bérenger, A perfectly matched layer for the absorption of electromagnetic waves, *Journal of Computational Physics* 114 (2) (1994) 185–200.
- [16] W.C. Chew, W.H. Weedon, A 3d perfectly matched medium from modified maxwell's equations with stretched coordinates, *Microwave and Optical Technology Letters* 7 (13) (1994) 599–604.
- [17] P. Chobea, D. Ecoti Aïe, G. Dutilleux, J. Picaut, An absorbing matched layer implementation for the transmission line matrix method, *Journal of Sound and Vibration* 337 (2015) 233–243.
- [18] T. Hagstrom, D. Givoli, D. Rabinovich, J. Bielak, The double absorbing boundary method, *Journal of Computational Physics* 259 (2014) 220–241.
- [19] J.-P. Bérenger, A historical review of the absorbing boundary conditions for electromagnetics, *Forum for Electromagnetic Research Methods and Application Technologies* 9 (6) (2015).
- [20] G. Montseny, J. Audounet, D. Matignon, Fractional integrodifferential boundary control of the Euler Bernoulli beam, *Conference on Decision and Control*, 1997, pp. 4973–4978.
- [21] S.-Y. Lee, C. Mote, Wave characteristics and vibration control of translating beams by optimal boundary damping, *Journal of Vibration and Acoustics* 121 (1) (1999) 18–25.
- [22] S.-Y. Lee, C. Mote, Vibration control of an axially moving string by boundary control, *Journal of Dynamic Systems, Measurement, and Control* 118 (1) (1996) 66–74.
- [23] P. Hagedorn, A. DasGupta, *Vibrations and Waves in Continuous Mechanical Systems*, Wiley, Chichester, UK, 2007.
- [24] L. Evans, *Partial Differential Equations, Graduate Studies in Mathematics*, American Mathematical Society, Providence, RI, 2010.
- [25] R. LeVeque, *Finite Difference Methods for Ordinary and Partial Differential Equations: Steady-State and Time-Dependent Problems* (Classics in Applied Mathematics Classics in Applied Mathemat), Society for Industrial and Applied Mathematics, Philadelphia, PA, USA, 2007.
- [26] D.W. Marquardt, An algorithm for least-squares estimation of nonlinear parameters, *Journal of the Society for Industrial & Applied Mathematics* 11 (2) (1963) 431–441.
- [27] C. Audet, J.E. Dennis Jr., Analysis of generalized pattern searches, *SIAM Journal on Optimization* 13 (3) (2002) 889–903.
- [28] K. Deb, D. Kalyanmoy, *Multi-Objective Optimization Using Evolutionary Algorithms*, John Wiley & Sons, Inc., New York, NY, USA, 2001.
- [29] K. Deb, A. Pratap, S. Agarwal, T. Meyarivan, A fast and elitist multiobjective genetic algorithm: NSGA-II, *IEEE Transactions on Evolutionary Computation* 6 (2) (2002) 182–197.
- [30] R. Higdon, Numerical absorbing boundary conditions for the wave equation, *Mathematics of Computation* 49 (179) (1987) 65–90.
- [31] L. Ljung (Ed.), *System Identification, Theory for the User*, 2nd ed. Prentice Hall PTR, Upper Saddle River, NJ, USA, 1999.
- [32] S.K. Lele, Compact finite difference schemes with spectral-like resolution, *Journal of Computational Physics* 103 (1) (1992) 16–42.
- [33] R.K. Shukla, M. Tatineni, X. Zhong, Very high-order compact finite difference schemes on non-uniform grids for incompressible Navier–Stokes equations, *Journal of Computational Physics* 224 (2) (2007) 1064–1094.
- [34] J.W. Kim, Optimised boundary compact finite difference schemes for computational aeroacoustics, *Journal of Computational Physics* 225 (1) (2007) 995–1019.
- [35] D. Rabinovich, D. Givoli, J. Bielak, T. Hagstrom, A finite element scheme with a high order absorbing boundary condition for elastodynamics, *Computer Methods in Applied Mechanics and Engineering* 200 (23–24) (2011) 2048–2066.
- [36] D. Baffet, J. Bielak, D. Givoli, T. Hagstrom, D. Rabinovich, Long-time stable high-order absorbing boundary conditions for elastodynamics, *Computer Methods in Applied Mechanics and Engineering* 241 (2012) 20–37.
- [37] K. Ogata, *Discrete-time Control Systems*, vol. 2, Prentice Hall, Englewood Cliffs, NJ, 1995.
- [38] S. Rao, *Vibration of Continuous Systems*, Wiley, Hoboken, NJ, 2007.
- [39] R. Courant, K. Friedrichs, H. Lewy, On the partial difference equations of mathematical physics, *IBM Journal of Research and Development* 11 (2) (1967) 215–234.
- [40] R. Marler, J. Arora, Survey of multi-objective optimization methods for engineering, *Structural and Multidisciplinary Optimization* 26 (6) (2004) 369–395.
- [41] M. Arnold, B. Simeon, Pantograph and catenary dynamics: a benchmark problem and its numerical solution, *Applied Numerical Mathematics* 34 (4) (2000) 345–362.
- [42] P.D. Welch, The use of fast Fourier transform for the estimation of power spectra: a method based on time averaging over short, modified periodograms, *IEEE Transactions on Audio and Electroacoustics* 15 (2) (1967) 70–73.
- [43] C.K. Tam, Computational aeroacoustics—issues and methods, *AIAA Journal* 33 (10) (1995) 1788–1796.
- [44] C. Bogey, C. Bailly, A family of low dispersive and low dissipative explicit schemes for flow and noise computations, *Journal of Computational Physics* 194 (1) (2004) 194–214.